



RESEARCH ARTICLE

10.1029/2023JD039818

Key Points:

- After controlling for convective available potential energy (CAPE), thunderstorms developing in dirty environments are 1.5 km deeper than storms developing in clean environments
- Controlling for CAPE, upper tropospheric ice water content is 50% greater for storms developing in dirty conditions versus clean conditions
- After controlling for CAPE, flash rates are a factor of two or more greater for storms developing in dirty conditions versus clean conditions

Correspondence to:

D. Allen,
djallen@umd.edu

Citation:

Allen, D., Pickering, K., Avery, M., Li, Z., Shan, S., Morales Rodriguez, C. A., & Artaxo, P. (2024). A CloudSat and CALIPSO-based evaluation of the effects of thermodynamic instability and aerosol loading on Amazon Basin deep convection and lightning. *Journal of Geophysical Research: Atmospheres*, 129, e2023JD039818. <https://doi.org/10.1029/2023JD039818>

Received 15 AUG 2023
Accepted 9 JAN 2024

Author Contributions:

Conceptualization: Dale Allen, Kenneth Pickering, Melody Avery, Zhanqing Li
Data curation: Dale Allen, Melody Avery, Carlos Augusto Morales Rodriguez, Paulo Artaxo
Formal analysis: Dale Allen, Kenneth Pickering, Melody Avery, Zhanqing Li
Funding acquisition: Dale Allen
Investigation: Dale Allen, Kenneth Pickering, Melody Avery, Zhanqing Li, Siyu Shan, Paulo Artaxo
Methodology: Dale Allen, Kenneth Pickering, Melody Avery, Zhanqing Li
Project Administration: Dale Allen

A CloudSat and CALIPSO-Based Evaluation of the Effects of Thermodynamic Instability and Aerosol Loading on Amazon Basin Deep Convection and Lightning

Dale Allen¹ , Kenneth Pickering¹ , Melody Avery² , Zhanqing Li^{1,3} , Siyu Shan¹ , Carlos Augusto Morales Rodriguez⁴ , and Paulo Artaxo⁵ 

¹Department of Atmospheric and Oceanic Science, University of Maryland, College Park, MD, USA, ²NASA Langley Research Center, Hampton, VA, USA, ³Earth System Science Interdisciplinary Center (ESSIC) University of Maryland, College Park, MD, USA, ⁴Instituto de Astronomia, Geofísica, e Ciências Atmosféricas, Universidade de Sao Paulo, Sao Paulo, Brazil, ⁵Instituto de Física, Universidade de Sao Paulo, Sao Paulo, Brazil

Abstract The Amazon Basin, which plays a critical role in the carbon and water cycle, is under stress due to changes in climate, agricultural practices, and deforestation. The effects of thermodynamic and microphysical forcing on the strength of thunderstorms in the Basin (75–45°W, 0–15°S) were examined during the pre-monsoon season (mid-August through mid-December), a period with large variations in aerosols, intense convective storms, and plentiful flashes. The analysis used measurements of radar reflectivity, ice water content (IWC), and aerosol type from instruments aboard the CloudSat and CALIPSO satellites, flash rates from the ground-based Sferics Timing and Ranging Network, and total aerosol optical depth (AOD) from a surface network and a meteorological re-analysis. After controlling for convective available potential energy (CAPE), it was found that thunderstorms that developed under dirty (high-AOD) conditions were 1.5 km deeper, had 50% more IWC, and more than two times as many flashes as storms that developed under clean conditions. The sensitivity of flashes to AOD was largest for low values of CAPE where increases of more than a factor of three were observed. The additional ice water indicated that these deeper systems had higher vertical velocities and more condensation nuclei capable of sustaining higher concentrations of water and large hydrometeors in the upper troposphere. Flash rates were also found to be larger during periods when smoke rather than dust was common in the lower troposphere, likely because smoky periods were less stable due to higher values of CAPE and AOD and lower values of mid-tropospheric relative humidity.

Plain Language Summary The Amazon Basin, which plays an important role in the carbon and water cycle, is under stress due to changes in climate, agricultural practices, and deforestation. The Basin includes a rainforest in the northwest and a mix of deforested areas, savannah-type vegetation, and agriculture in the southeast. The effects of instability and aerosol loading on thunderstorms in the Basin (75–45°W, 0–15°S) were examined during mid-August through mid-December, a period with large variations in aerosols, intense convective storms, and plentiful flashes. The analysis used measurements of radar reflectivity, ice water content (IWC), and aerosol type from instruments aboard the CloudSat and CALIPSO satellites, flash rates from the ground-based Sferics Timing and Ranging Network, and AOD from a surface network and a meteorological re-analysis. After controlling for convective available potential energy, a measure of instability, it was found that thunderstorms that developed under dirty (high-AOD) conditions were approximately 1.5 km deeper, had 50% more IWC, and more than two times as many flashes as storms that developed under clean (low-AOD) conditions. Flash rates were also found to be larger during periods when smoke rather than dust was common in the lower troposphere, likely because these periods were less stable.

1. Introduction

Deep convection requires low-level convergence, boundary layer moisture, and instability. Tao et al. (2012), Li et al. (2017, 2019), and Fan and Li (2022) review the intimate connection between aerosols and deep convection. Many aerosol particles are hygroscopic and serve as efficient cloud condensation nuclei (CCN) when activated. Activated cloud droplets grow by both condensation and coalescence, with the much faster coalescence process becoming increasingly important as cloud droplets rise through the cloud and grow (Freud et al., 2011; Freud & Rosenfeld, 2012; McFiggans et al., 2006). The height cloud droplets must reach before coalescence dominates

© 2024. The Authors.

This is an open access article under the terms of the [Creative Commons Attribution License](https://creativecommons.org/licenses/by/4.0/), which permits use, distribution and reproduction in any medium, provided the original work is properly cited.

Resources: Dale Allen, Melody Avery, Zhanqing Li, Carlos Augusto Morales Rodriguez

Software: Dale Allen, Melody Avery

Supervision: Dale Allen, Kenneth Pickering, Melody Avery, Zhanqing Li

Validation: Dale Allen

Visualization: Dale Allen

Writing – original draft: Dale Allen

Writing – review & editing: Dale Allen, Kenneth Pickering, Melody Avery,

Zhanqing Li, Siyu Shan, Carlos Augusto

Morales Rodriguez, Paulo Artaxo

over condensation increases with aerosol optical depth (AOD) (Zhu et al., 2015). Therefore, the onset of coalescence in convection occurring at polluted locations may be delayed until droplets rise to altitudes where temperatures are sub-freezing, and glaciation is possible (Rosenfeld et al., 2008). The effect of this delay is a suppression of warm rain and an invigoration of deep convection and lightning (Khain et al., 2005; Koren et al., 2005, 2010; Y. Liu et al., 2020; Lohmann, 2008; Li et al., 2011; Niu & Li, 2012; Petersen & Rutledge, 2001; Yang & Li, 2014). Within a convective mixed-phase layer, interactions between graupel and ice crystals in the presence of supercooled water lead to efficient charge transfer, electric field growth, and lightning (Blyth et al., 2001; Saunders et al., 2006; Takahashi, 1978).

Observations and numerical simulations suggest that adding aerosols to a pristine environment intensifies deep convection through aerosol-induced changes in the mixed phase layer of the cloud that enhance lightning (Fan et al., 2018; Sun et al., 2023, 2024). As the aerosol amount continues to increase, a larger population of tiny droplets begins to suppress the growth of graupel and the delivery of large, supercooled droplets to the mixed phase region thus suppressing charge separation and flash rates (Williams et al., 2002). For larger aerosol amounts, the aerosol invigoration effect is opposed by an aerosol radiative forcing effect that stabilizes the atmosphere and lessens the intensity of deep convection (Andreae et al., 2004; Koren et al., 2008; Manoj et al., 2021; Rosenfeld, 1999; Wang et al., 2013; Williams et al., 2002; Yang et al., 2013; Yuan et al., 2011). The combined impact of the opposing effects under polluted conditions may delay the development of intense storms until later in the day (Guo et al., 2016; Lee et al., 2016) and can lead to increases or decreases in rainfall depending on atmospheric humidity, buoyancy, and windshear (Khain, 2009). Albrecht et al. (2011) found that aerosols enhanced lightning activity in the Amazon Basin, but the effect was statistically significant only during the wet season. Fan et al. (2009, 2016) found that microphysical invigoration is largest in moist environments with minimal wind shear, warm cloud bases, and ample convective available potential energy (CAPE) such as the tropical western Pacific and southeastern China. Storer et al. (2014) examined the sensitivity of four CloudSat deep convective parameters to AOD over the eastern North Atlantic using CloudSat data for 2006–2009 and aerosol fields from an aerosol assimilation system (Hollingsworth et al., 2008). After controlling for CAPE and lower tropospheric static stability (LTSS), they found that increases in the radar reflectivity centroid (Z_{re}) (Heiblum et al., 2012; Koren et al., 2009), cloud top height, rain top height (highest layer for which radar reflectivity (Z_e) > 0), and ice water path (IWP) with AOD were statistically significant both in deep convective cores and in the surrounding stratiform region. Buiat et al. (2017) examined the characteristics of clouds conducive to lightning formation using CloudSat products and lightning data from 12 convective events over Italy. They found a strong correlation between the number of strokes and the vertical distribution of ice particles, with lightning discharges most common when ice water content (IWC) and effective radius values were large at mid-and-upper levels (Takahashi, 1978). Peng et al. (2016) examined the sensitivity of deep convective cloud heights to aerosol loading using aerosol amounts from Moderate Resolution Imaging Spectrometer (MODIS) and cloud top heights from CloudSat. They found that tropical cloud top heights over land increased by 2–4 km as AOD increased from 0.1 to 0.5, with larger increases for mixed-phased clouds with warm bases ($T > -15^\circ\text{C}$) than for mixed-phase clouds with cold bases. An aerosol invigoration signal was not found in several other studies. For example, Veals et al. (2021) examined the impact of aerosols on the depth of deep convective storms using measurements from the Cloud, Aerosol, and Complex Terrain Interactions campaign that took place from October 2018 to April 2019 in central Argentina. They found that the 15 dBZ echo top height increased strongly with the level of neutral buoyancy and with CAPE. Echo top heights also increased with AOD; however, after accounting for correlations with meteorological variables, increasing AOD was generally correlated with higher cloud top temperatures and a decrease in the vertical extent and intensity of deep convection. Grabowski and Morrison (2020) used a model to examine convective development over Amazonia. They found that adding additional ultrafine CCN led to increased cloud buoyancy, stronger updrafts, and thus more condensation below the freezing level; however, they did not observe what is traditionally called convective invigoration, that is, an impact at altitudes above the freezing level.

The Amazon Basin is an area that includes the Amazon rainforest in the northwest and a mix of deforested areas, savannah-type vegetation, and agriculture in the southeast (Kumar et al., 2023; Ter Steege et al., 2013). Climate change and deforestation are affecting the air quality and weather, increasing the Basin's susceptibility to drought, especially in the southeastern portion of the Basin (Wunderling et al., 2022). Biomass burning associated with agricultural practices and deforestation enhances the concentration of aerosols (Mataveli et al., 2021), especially during the dry season when mean concentrations of particles are 10 times greater than during the



Figure 1. Map showing region of interest. The Amazon Basin (75°–45°W, 15°–0°S) is highlighted with a black rectangle. The locations of the nine Aerosol Robotic Network sites used in this study are shown with blue stars.

wet season (Artaxo et al., 2002, 2022). Changes in the thermodynamic environment associated with this drying are also impacting the abundance of smoke and dust in the atmosphere, the amount of rainfall (Saad et al., 2010), and the frequency and intensity of deep convection and lightning (Albrecht et al., 2011; Altaratz et al., 2010; Morales-Rodriguez, 2019). Therefore, this region is an ideal location to study the evolving relationship between thermodynamics, microphysics, aerosol amounts, precipitation rates, and ultimately flash rates.

Albrecht et al. (2011) examined variations in convective intensity during the mid-September to mid-November transition between dry and wet seasons over Rondonia. They found that storms were more intense (i.e., had higher percentages of positive cloud-to-ground (+CG) flashes, and higher 30 dBZ echo top heights) during the dry season (mid-September to early October at this location) than the transition or wet seasons. They also found that the intensity of storms was independent of aerosol concentrations early in the period when aerosol concentrations were high but increased with aerosol concentrations beginning October 20th, when lower concentrations

of aerosols allowed an aerosol-limited regime to be established. Wall et al. (2014) studied the impact of aerosols on convective features over the Amazon, central Africa, the tropical Atlantic, and the North American Monsoon regions using 10 years of Tropical Rainfall Measuring Mission (TRMM) Precipitation Radar data on convective storms and 5 years of CloudSat data on cumulus congestus clouds. In the Amazon Basin, they found that convective storms forming in more polluted conditions based on MODIS aerosol index values had 30% more rain, 4.5 × more lightning, 2 km higher cloud tops as determined using the metric maximum height of 20 dBZ echo, and more ice scattering (85-GHz polarization-corrected temperatures were 9 K lower) than storms forming over clean regions. Stolz et al. (2015) examined the impact of thermodynamics and aerosols on the intensity of deep convection and flash rates using data on convective features observed by TRMM. They found that the lightning density decreased with warm cloud depth (WCD), that is, the vertical thickness between the lifting condensation level and the freezing level. When WCD was held constant, total lightning density over continents increased by approximately 170% between low and high values of aerosols with diameters greater than 40 nm (N40). Altaratz et al. (2017) studied the link between aerosol loading and convective activity over several regions including the Amazon. Over the Amazon, they found that Worldwide Lightning Location Network flash densities (Virts et al., 2013) in polluted air exceeded those in clean air by approximately a factor of two during March–May 2012 for CAPE values between 500 and 2,500 J kg⁻¹. Jiang et al. (2018) examined the impact of aerosol type on the intensity of deep convection over three regions of the globe including South America (0°–30°S, 35°–80°W). Over South America, they found that values of the IWC centroid (Z_{IWC}) were lower when the CALIOP aerosol type Elevated Smoke (ES) was dominant and higher when Polluted Continental Smoke (PCS) was dominant. The response of Z_{IWC} to aerosol perturbations was found to be non-monotonic consistent with several studies that show a turning point in the response of convective metrics and flashes to AOD due to the competing influences of microphysical and radiative effects (Wang et al., 2018).

In this study, the relationship between aerosols, deep convection, precipitation, and lightning is examined over the Amazon Basin (75°–45°W, 0°–15°S) (see Figure 1) using CAPE from the ERA5 reanalysis, total column optical depth from Aerosol Robotic Network (AERONET) (Palacios et al., 2022) and the Modern-Era Retrospective analysis for Research and Applications (MERRA-2) reanalysis (Buchard et al., 2017), precipitation rates from Integrated Multi-satellitE Retrievals for Global Precipitation Mission (IMERG) (Huffman et al., 2019, 2020), flash rates from the Sferics Timing and Ranging Network (STARNET) (Morales-Rodriguez et al., 2011), estimates of convective intensity and aerosol type derived from CloudSat (Stephens et al., 2002) and CALIPSO (Winker et al., 2009, 2010), and profiles of relative humidity (RH) and temperature obtained from ancillary European Center for Medium-Range Weather Forecasts (ECMWF) products (Cronk & Partain, 2017). This study expands on these previous studies that examine the combined impact of thermodynamics and aerosols on the intensity of deep convection in the Amazon Basin. Section 2 describes the data products and methodology, Section 3 examines the sensitivity of convective intensity to observed and reanalysis-based estimates of total column AOD after controlling for CAPE, and Section 4 offers conclusions.

2. Methodology and Data Products

This study focuses on the pre-monsoon period defined here to be August 16 to December 15. This period is focused on because it has large variations in aerosols, continental conditions, and high lightning activity (Petersen & Rutledge, 2001; Saraiva et al., 2017). It is a period when the CAPE threshold for deep convective storms is low, and the percent of clouds that are cumulonimbus is the largest (Wu & Lee, 2019). In addition, more thunderstorms form during this period because it is a transition period that occurs after aerosol sources have built up over the dry season but before the most intense rainfall (monsoon). The onset of the rainy season in the Amazon Basin varies with location and year but can begin as late as mid-December (Marengo et al., 2001). The range of years examined is 2012–2017. This time period was chosen because it is a period with flash data from STARNET that encompasses CloudSat Epoch 6 that began on 15 May 2012 when CloudSat returned to the A-Train formation enabling overlap with ancillary data from MODIS and CALIPSO and ended in early 2018 when CloudSat exited the A-train. In this study, CloudSat daytime data are available for 15 May 2012, through 5 December 2017, while CALIPSO data used in estimating the aerosol type are available for most days during the 2012–2017 time period.

2.1. CloudSat Products

CloudSat is a satellite launched in April 2006 that carries a radar capable of penetrating cloud tops and examining the internal structure and microphysics of deep convective clouds (Stephens et al., 2002). CloudSat with an equator crossing time of 1:30 p.m. during the period of this study contains a W-band (94-GHz) nadir-looking Cloud Profiling Radar (CPR) with a 1.1 km footprint and a 480 m vertical resolution that can be used to observe relatively small cloud hydrometeors (Tanelli et al., 2008). The primary CloudSat variables used in this study are profiles of cloud type from the 2B-CLDCLASS data set (Sassen & Wang, 2008), profiles of radar reflectivity (Z_e) obtained from the 2B-GEOPROF data set (Mace & Zhang, 2014; Marchand et al., 2008; Protat et al., 2009) and profiles of IWC (Deng et al., 2013, 2015) obtained from the 2C_ICE product. The product version used in this study is Revision 05. The 2C-ICE product uses Z_e along with attenuated backscattering coefficients at 532 nm (γ') from the CALIPSO lidar (see Section 2.2) to constrain the ice cloud retrieval more tightly than a radar-only product that is also available but not used in this study. The microphysically constrained ice water path (IWP-IP) (g m^{-2}) is also read in from the 2C_ICE data sets and used in the analysis. The centroid or center-of-gravity of IWC (Z_{IWC}) is calculated by weighting the altitude of the CloudSat layers (Z) by the IWC (Jiang et al., 2018). Mathematically,

$$Z_{\text{IWC}} = \frac{\sum_{k_1}^{k_2} \text{IWC}(k) \cdot Z(k)}{\sum_{k_1}^{k_2} \text{IWC}(k)}$$

where the summations start at the above-ground CloudSat layer with the highest value of Z_e (K_1) and end with the highest CloudSat cloud layer (K_2). Similarly, the centroid of radar reflectivity (called Z_{re} here but the center of gravity by Storer et al., 2014) is calculated by weighting Z by the radar reflectivity (Z_e). Mathematically,

$$Z_{\text{re}} = \frac{\sum_{k_1}^{k_2} Z_e(k) \cdot Z(k)}{\sum_{k_1}^{k_2} Z_e(k)}$$

where the summation starts at the above-ground CloudSat layer with the highest value of Z_e (K_1), ends with the highest CloudSat cloud layer (K_2), and only includes layers for which Z_e is greater than zero.

The metrics Z_{IWC} and Z_{re} are used to assess the intensity of deep convective systems sampled by CloudSat and CALIPSO. To compare the intensity of systems, representative values of Z_{IWC} and Z_{re} were determined for each deep convective system observed by CloudSat during the 2012–2017 time period. The CloudSat algorithm determines the cloud type using information that includes the maximum Z_e measured by the CPR, the presence of precipitation, the temperature profile, and the height of surface topography (Marchand et al., 2008; Sassen & Wang, 2008). Only profiles with clouds typed as deep convective are used in this study. Deep convective clouds were present in 3% of CloudSat profiles over Amazonia (Dodson et al., 2018). A deep convective system is defined here to consist of five or more adjacent CloudSat profiles that contain at least one layer that is typed as deep convective by CloudSat. However, the adjacency requirement is waived if two groups of deep convective retrievals are separated by just one retrieval that does not contain a deep convective layer. In that instance, the two groups are combined into one system. The location of each system is obtained by averaging the latitude and

longitudes of individual profiles within the system. Similarly, representative values of convective metrics, including Z_{IWC} and Z_{re} , are obtained for each system by averaging values from the individual retrievals. Means are used instead of maxima because maxima are sensitive to the number of profiles in a system, which varies significantly between convective systems.

2.2. CALIPSO Products

In addition to the CloudSat radar, the companion satellite CALIPSO (Winker et al., 2009, 2010) contains a lidar (Hunt et al., 2009) for use in examining the properties of clouds and aerosols in detail. In this study, information from CALIPSO is incorporated into the estimate of IWC and IWP (see Section 2.1) and is critical in estimating the type of aerosol present when deep convective systems develop. In this study, we used both daytime and nighttime v4.2 Lidar Level 2 CALIPSO aerosol types (Kim et al., 2018; Omar et al., 2009). Important CALIPSO variables used in estimating the aerosol type are the Level 1 estimated particulate depolarization ratio (δ_p) and the Level 1 532 nm integrated attenuated backscatter (γ') (Kim et al., 2018). γ' is useful for determining how much aerosol is present in an aerosol layer, while δ_p is useful for determining the sphericity of aerosol particles. In optically thin aerosol layers, the depolarization ratio is a measure of how much the particle surface is faceted, with larger values indicating that the particles are less smooth, or spherical. Over land, CALIOP layers with $\delta_p > 0.20$ are assumed to be Dust, while layers with $0.075 < \delta_p < 0.20$ are assumed to be Polluted Dust. Layers over land with $\delta_p < 0.075$ and $\gamma' < 0.0005$ are assumed to be Clean Continental, while layers with $\delta_p < 0.075$ and $\gamma' > 0.0005$ are assumed to be ES if the top of the aerosol layer (Z_{top}) is located above 2.5 km and PCS for $Z_{top} < 2.5$ km. A small percentage of grid boxes in the northeastern portion of the study region are located over water. See Kim et al. for more details on how aerosol typing is done for these retrievals. While considerable effort has gone into evaluating and refining CALIOP aerosol types (e.g., Mielonen et al., 2009; Papagiannopoulos et al., 2016), the information available to discriminate aerosol types is limited. For example, the only difference between PCS and ES is the altitude of the aerosol layer, while the only difference between Dust and Polluted Dust is the value of δ_p .

Since mid-2016, an increasing percentage of the pulses emitted by the CALIPSO lidar have been low energy due to pressure losses in the canister housing the laser (Tackett et al., 2022). Low energy CALIPSO retrievals, that is, retrievals with energies of less than 0.08 J, occur most frequently in the South Atlantic Anomaly, a high radiation region that includes the southern portion of the Amazon Basin. Low-energy shots were rare in the Amazon Basin until August 2016. Figure 2 shows the time series of the low-energy shot frequency for $5^\circ \times 5^\circ$ regions in the Amazon Basin over the 2016–2017 time period. For the August 2016 to December 2017 period, the percentage of low-energy shots ranged from 20% to 30% in the northern portion of the Basin to 40%–55% in the southern portion of the domain. By late 2017, the percentage of low-frequency shots was 30%–50% in the northern Basin and 50%–80% in the southern Basin. Low-energy CALIOP retrievals are of lower quality and are not used in this study as recommended by the CALIPSO team. A minor consequence of the increase in low-energy shots is that the aerosol typing used in this study is biased toward 2012–2015 when more data are available.

When possible, the dominant aerosol type is identified for each deep convective system using only high-energy (>0.08 J), high-confidence extinction retrievals. As suggested by the CALIPSO team (Z. Liu et al., 2018; Tackett et al., 2018; Vaughan et al., 2009), we filtered the aerosol profiles to include extinction quality flags of 0 or 1, indicating semi-transparent aerosol layers and 16 or 18 indicating opaque aerosol layers (see Section 5.3.1 of Tackett et al., 2018). We included layers with Cloud-Aerosol-Discrimination (CAD) scores between -100 and -20 inclusive. CAD scores range from -100 to 100 , with -100 indicating complete confidence that a feature is an aerosol and a value of 100 indicating complete confidence that a feature is a cloud. When possible, the CALIOP data set contains an estimate of the aerosol type for each layer. To estimate the dominant aerosol type associated with each convective system, we extracted all nighttime and daytime CALIOP retrievals within the $1^\circ \times 1^\circ$ grid box containing the system on the day of the system. We then examined the aerosol type for all layers with pressures greater than 675 hPa. The pressure threshold is set to 675 hPa, ~ 3 km for a convective boundary layer because the air from higher layers of the atmosphere is less likely to be ingested into a storm and affect its development. The most common aerosol type was then assumed to be representative of the grid box and convective system. One of the caveats of this simplistic approach for determining the aerosol type associated with each system is that it does not consider the amount of aerosol in each layer, intra-day variations in aerosol type, the impact of multiple aerosol layers of different types, or give weight to variations in the horizontal resolution (5, 20, or 80 km) of the retrieved layers.

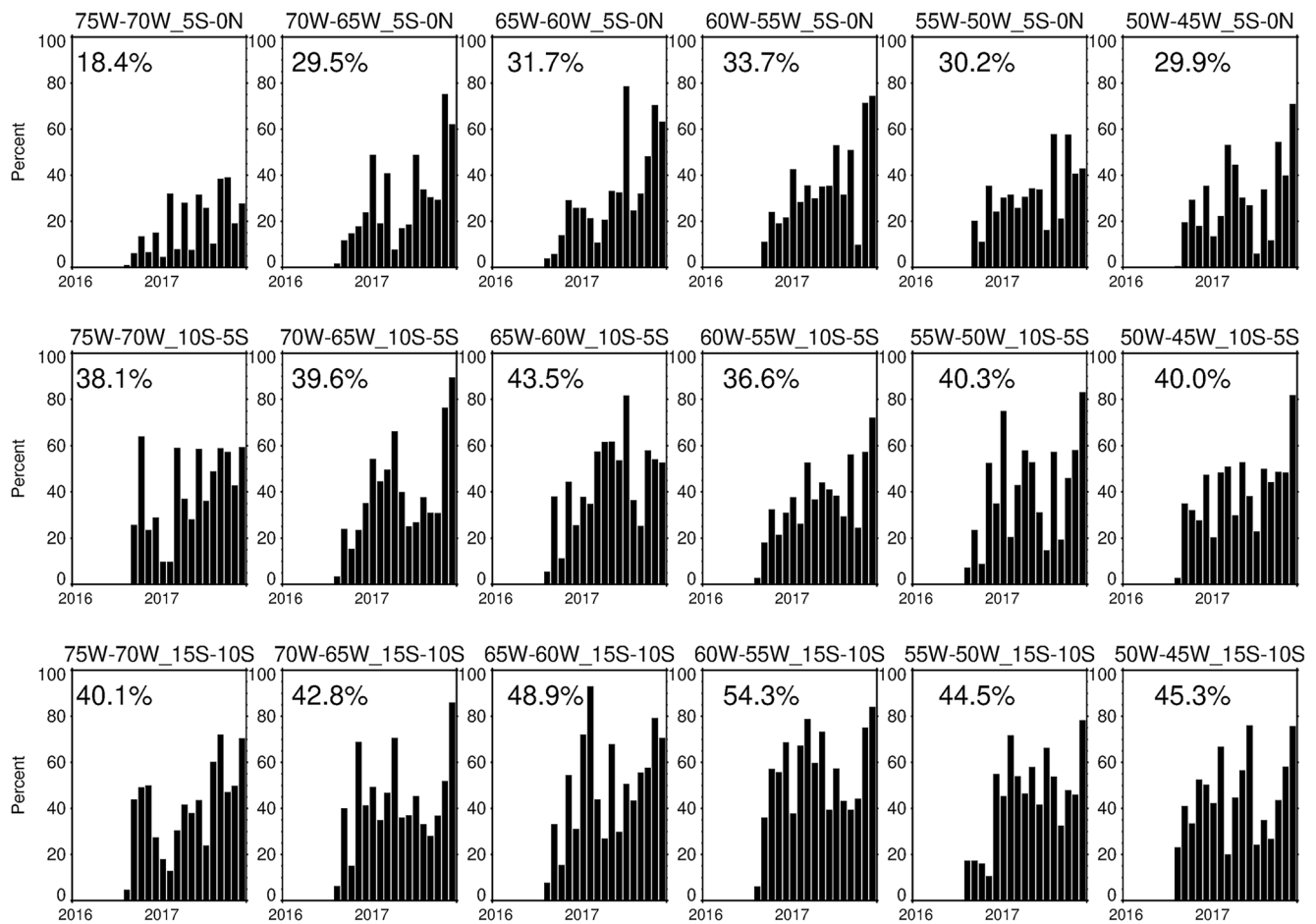


Figure 2. Time series showing percent of CALIOP shots that are low-energy ($<0.08\text{ J}$) as a function of month over the 2016–2017 time period. Values are shown for $18\ 5^\circ \times 5^\circ$ grid boxes within the Amazon Basin. The percentages shown in the upper left of each plot are means over the August 2016–December 2017 time period.

Using the v4.2 CALIPSO AOD retrieved for each aerosol layer, we determined aerosol loading by dust and smoke. By summing the AOD values for lower tropospheric layers typed as Polluted Dust, Dust, and Dusty Marine, an estimate of the AOD due to dust was obtained for each profile (AOD_Dust). By summing the AOD values for layers typed as ES and PCS, each profile obtained an estimate of the AOD due to smoke (AOD_Smoke). The sums from all profiles on a given day were averaged to obtain an estimate of the AOD due to smoke and dust on that day. Time series of bimonthly mean AOD_Dust and AOD_Smoke for the 2012–2017 time period are shown in Figure 3 described in more detail in Section 3.1).

2.3. Thermodynamic Metrics

CAPE, an indicator of the instability of the atmosphere, was used to identify large-scale environments favorable for the development of intense storms with lightning (N. Liu et al., 2020). CAPE is often used in conjunction with other variables, such as updraft velocity or precipitation to estimate flash rates (Choi et al., 2005; Romps et al., 2014) or IC fraction (Shan et al., 2023). Gridded hourly values of CAPE are available at $0.25^\circ \times 0.25^\circ$ resolution from the ERA5 reanalysis (Hersbach et al., 2020) that was produced by blending ECMWF forecasts with observations using four-dimensional variational data assimilation. For each deep convective system, CAPE was extracted in the $1^\circ \times 1^\circ$ grid box containing the system for the three-hour period ending at the time of the CloudSat overpass. The maximum of the three-hourly values was taken, assumed to be representative of the thermodynamic environment, and will be used in this analysis.

The intensity of deep convective storms also varies with LTSS and mid-tropospheric RH (Wall et al., 2014). LTSS is defined as the potential temperature difference between the surface and 700 hPa, and mid-tropospheric

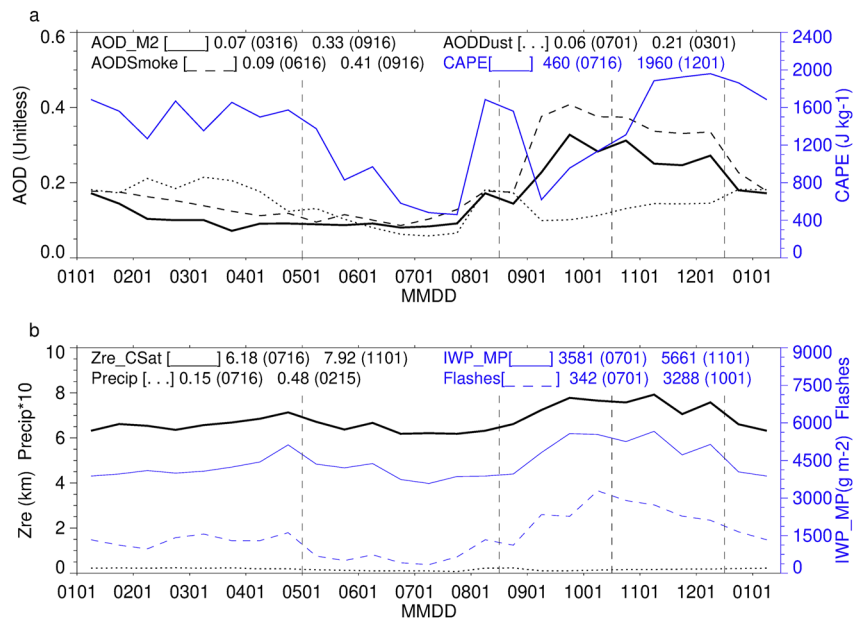


Figure 3. Time series showing bi-monthly means of selected variables constructed from days in 2012–2017 with CloudSat and CALIPSO retrievals in the Amazon Basin. (a) Shows Modern-Era Retrospective analysis for Research and Applications-2 aerosol optical depth (AOD) (solid black line), CALIOP AOD from dust (dotted black line), CALIOP AOD from smoke (dashed black line), and ERA5 convective available potential energy (CAPE) (solid blue line). (b) Shows CloudSat Z_{re} (solid black line), CloudSat and CALIPSO-based ice water path (IWP) (solid blue line), Integrated Multi-satellitE Retrievals for Global Precipitation Mission precipitation (dotted black line), and Sferics Timing and Ranging Network flashes (dashed blue line). The method used to obtain values for AOD_Smoke and AOD_Dust is described in Section 2.2. Daily CAPE values obtained by taking 90th PCTL of 3-hour maximum values (17–19 UTC) over Basin. Daily flash values obtained by summing flashes over Basin during the 10-min time periods that contains CloudSat overpass. Daily precipitation values are mean precipitation rates over Basin during 30-min time periods containing CloudSat overpass. Daily AOD values are mean values over Basin during one-hour time period containing CloudSat overpass. Daily Z_{re} values are mean values of Z_{re} for deep convective systems observed that day over Basin. Daily IWP values obtained by taking maximum of mean IWP values for CloudSat-CALIPSO profiles of deep convective systems within Basin.

RH is defined as the mean RH of deep convective cloud layers between 3 and 7 km above mean sea level. Temperature and RH profiles corresponding to the CloudSat cloud profiling bins were read from version P1_R05 of the ECMWF-AUX data set (Cronk & Partain, 2017).

2.4. Metrics of Aerosol Loading

Information on the total column aerosol amount over Amazonia was obtained from the AERONET (Andreae et al., 2015; Estevan et al., 2019; Holben et al., 2001; Palacios et al., 2022) and version two of the MERRA (Gelaro et al., 2017).

AERONET is a ground-based remote sensing aerosol network that provides column AOD data at numerous global locations. The network has nine locations with extensive Amazon Basin data during the 2012–2017 time period (Table 1). This study uses version 3 AERONET AOD values with Spectral Deconvolution Algorithm (SDA) Retrieval Level 2. These values are cloud-cleared and quality assured with pre-field and post-field calibrations applied. The seasonality of aerosol optical properties over the Amazon is discussed in Schafer et al. (2008). They find low concentrations of aerosols throughout the Basin during the first half of the year with dramatic increases, especially in the southern forested region and the adjacent cerrado (woodland/savanna) region to its east, with the onset of the burning season in September.

The MERRA-2 system includes the Goddard Chemistry, Aerosol, Radiation and Transport model (Chin et al., 2002) integrated into version 5 of the Goddard Earth Observing System Model (GEOS-5) and an assimilation system that assimilates meteorological parameters as well as aerosols (Buchard et al., 2017). Aerosol products that are assimilated include AOD from advanced very high-resolution radiometer, MODIS (Remer

Table 1
Aerosol Robotic Network Sites Used in This Analysis

Location	Longitude	Latitude	First day with observations	Last date with observations	Days ^a	Obs ^b
Huancayo-IGP	75.32°W	12.04°S	20 Mar 2015	30 Dec 2017	298	11,990
Rio Branco	67.87°W	9.96°S	16 Jan 2012	30 Oct 2017	347	3,875
Ji Parana SE	61.85°W	10.93°S	1 Jan 2012	29 Dec 2017	379	4,073
Manaus EMBRAPA	59.97°W	2.89°S	1 Jan 2012	28 Dec 2017	337	3,049
ARM Manacapuru	60.60°W	3.21°S	20 Dec 2013	30 Nov 2015	83	835
Amazon ATTO Tower	59.00°W	2.14°S	10 Mar 2016	29 Dec 2017	149	1,116
<i>Greater Manaus^c</i>	59.86°W	2.78°S	1 Jan 2012	29 Dec 2017	429	5,000
Alta Floresta	56.10°W	9.87°S	28 Jan 2012	31 Dec 2017	406	3,915
Cuiaba-Miranda	56.07°W	15.73°S	3 Jan 2012	30 Dec 2017	394	4,158
Brasilia-SONDA	47.71°W	15.60°S	16 Sep 2015	7 Dec 2016	107	1,119

^aDays refers to the number of days during 2012–2017 with observations during the pre-monsoon period. ^bObs refers to the number of observations during the pre-monsoon period. ^c*Greater Manaus* is a fictional site created using measurements from the Manaus EMBRAPA site, the ARM Manacapuru site that was active during the GoAmazon experiment (Martin et al., 2017), and the Amazon Tall Tower Observatory (ATTO) that has been active since March 2016 (Andreae et al., 2015). The ATTO tower is upwind of the city of Manaus (>1 million population). EMBRAPA is in/near the city, and the ARM site was downwind of the city.

et al., 2008), Multi-angle Imaging Spectro-Radiometer (Kahn et al., 2005) over bright surfaces, and AERONET (Randles et al., 2017). The distributions of organic carbon, black carbon, sea salt, dust, and sulfate aerosols are output by the MERRA-2 system. Hourly $0.625^\circ \times 0.5^\circ$ horizontal resolution MERRA-2 AOD was used in this study (GMAO, 2015). For each deep convective system, the MERRA-2 AOD was extracted at the location of the centroid of the system in the hour containing the CloudSat/CALIPSO overpass and is assumed to be representative of the system. It is important to note that the MERRA-2 AOD is a total column, which includes the stratosphere. Thus, the MERRA-2 column could be impacted by stratospheric aerosols that are unlikely to be ingested into a convective storm.

2.5. Precipitation and Lightning Products

Precipitation data were taken from the IMERG (Huffman et al., 2019, 2020). The IMERG algorithm merges intercalibrated estimates of precipitation from passive microwave and infrared sensors aboard the TRMM (2000–2014) and GPM (2014–present) satellites, precipitation gauges, and other sources to estimate the rain rate at a 30-min temporal and $0.1^\circ \times 0.1^\circ$ horizontal resolution. The quality of the IMERG data product over the Amazon Basin is discussed in Oliveira et al. (2016) and Sapucci et al. (2022). In general, they find that IMERG captures the main aspects of the rainfall distribution including its diel cycle. However, IMERG underestimates the frequency of both light ($<0.4 \text{ mm hr}^{-1}$) and heavy rain events ($>10 \text{ mm hr}^{-1}$). The latter bias may be caused by TRMM and GPM's inability to detect intense and localized rain cells. These limitations add uncertainty to estimates of the effect of aerosols on rain rate. However, mean rain rates of both clean and dirty storms will be affected by this bias limiting its impact. In this application, we use the gridded L3 research quality final product, which has been calibrated using monthly rain gauge data. For use with other products, the $0.1^\circ \times 0.1^\circ$ 30-min resolution IMERG precipitation was aggregated onto a $1^\circ \times 1^\circ$ grid over the 2012–2017 time period.

Lightning flashes were provided by the South American VLF long-range lightning detection network known as STARNET (Morales-Rodriguez et al., 2014). STARNET is a ground-based network composed of 13 VLF sensors distributed over South America (9 sensors), North America (1), the Caribbean (1), and Africa (2) that measure sferics (radio noise emitted by lightning discharges). To determine the lightning location, STARNET uses the arrival time difference method that requires at least four sensors (Morales-Rodriguez et al., 2014). This lightning network detects mostly cloud-to-ground strokes of both polarities. These strokes are clustered into flashes using a time and space constraint proposed by Cummins et al. (1998), that is, 1 s and 15-km. STARNET has a stroke detection efficiency of 35% ($\sim 70\%$ for flashes) and a location error varying from 2 to 5 km over South America (Morales-Rodriguez et al., 2014). In this analysis, CG flashes are used as a proxy for total flashes. This assumption adds uncertainty because the mean IC fraction in the Amazon Basin ranges from 50 to 90+ %. This

assumption is necessary because continuous measurements of IC flashes were not available during the time of this study and are just now becoming available in the region, via GLD360 (Said et al., 2013) for example. Fortunately, there is a strong relationship between IC and CG flashes. For most applications, flashes for the 2012–2017 time period are read in for each day and gridded at a 10-min temporal and a $0.1^\circ \times 0.1^\circ$ horizontal resolution. Flash counts are not adjusted for detection efficiency, and all flashes are included regardless of the value of the quality control flag. For comparison with IMERG precipitation and other variables, STARNET flashes were accumulated over 30-min periods and aggregated onto the same $1^\circ \times 1^\circ$ grid.

3. Results

3.1. Climatological Variations in Variables of Interest Over the Amazon Basin

Figure 3a shows seasonal variations of CAPE and AOD; variables that affect the intensity of deep convection, while Figure 3b shows variations in metrics of convective intensity, specifically IWP, the centroid of Z_e (Z_{re}), precipitation, and flashes. The mean values of CAPE range from 460 J kg^{-1} during July to $1,960 \text{ J kg}^{-1}$ at the beginning of the wet season in early December. In general, CAPE increases between July and December; however, it has a secondary peak during late August and early September, likely explaining a secondary maximum in precipitation observed during the same period. AOD is lowest during March and remains low through July. It then increases from August through September and remains high until the onset of the wet season in December. AOD from low-level smoke exceeds AOD from low-level dust by about 60%. Thus, the AOD seasonal cycle is driven by smoke, which is at a minimum in late June and maximizes in late September. The distributions of IWP and Z_{re} are very similar because the IWC values used in the integration to obtain IWP were derived from a combination of Z_e and the CALIPSO lidar attenuated backscatter (Deng et al., 2013). Except for rainfall, the convective intensity metrics have minima during the dry season (late July), increase through the early pre-monsoon period, and decrease slowly during the latter portion of the pre-monsoon season. Precipitation is also lowest during July, but it shows a broad maximum during the wet season and the aforementioned peak in late July and early August.

3.2. Sensitivity of Precipitation and Flash Rates to CAPE and Aerosol Loading

Contrasts in AOD, CAPE, rain rate, and lightning flashes between 30-min periods with low- and high-aerosol loading (clean and dirty periods) were examined for the pre-monsoon period using time series of MERRA-2 AOD, ERA5 CAPE, IMERG precipitation, and STARNET flashes for each of $450 \text{ } 1^\circ \times 1^\circ$ grid boxes within the Amazon Basin. Time series of precipitation and flashes were calculated by averaging $0.1^\circ \times 0.1^\circ$ gridded values over 30-min periods. The archived temporal resolution of ERA5 CAPE and MERRA-2 AOD is one-hour. Values for 30-min periods were obtained by replicating hourly values obtained by averaging values from ERA5 and MERRA-2 grid boxes within the $1^\circ \times 1^\circ$ grid boxes. The resulting time series for each of the 450 grid boxes were then filtered to remove periods without flashes and also periods with precipitation rates of less than 0.001 mm hr^{-1} .

Figures 4a–4d are probability distribution functions showing median changes in AOD, CAPE, precipitation, and lightning flashes between clean and dirty 30-min periods during the pre-monsoon I (August 16–October 15) time period. By definition, the change in AOD must be positive, as AOD was used in separating clean and dirty periods. Overall, the median AOD when dirty was a factor of 3 greater than the median AOD when clean. The median increase in CAPE between clean and dirty periods was a relatively small 123 J/kg (8%), with positive changes over 69% of the Basin. Overall, the median rain-rate increased by 0.15 mm hr^{-1} (65%), with 89% of the Basin having more rain when dirty. The IMERG rain rate is available at $0.1^\circ \times 0.1^\circ$ resolution for each of the 450 $1^\circ \times 1^\circ$ grid boxes. The median, mean, and maximum $0.1^\circ \times 0.1^\circ$ rain rate within each $1^\circ \times 1^\circ$ grid box and the fraction of $0.1^\circ \times 0.1^\circ$ grid boxes with rain were calculated and averaged to obtain values for clean and dirty periods. The 65% increase in mean precipitation between clean and dirty periods was accompanied by a 34% increase in the maximum precipitation rate and a 28% increase in the fraction of grid boxes with precipitation during a given 30-min period. Thus, both the intensity and area of the rain increased. The median flash rate increased by a relatively modest 5.7 flashes (23%), with a large percentage (74%) of the Basin having more flashes when dirty. Increases in flash rate were greatest and mostly spatially coherent in the northern portion of the domain. The values quoted above were obtained using fields from all hours of the day. To determine if the results were an artifact caused by diel variations, the changes were also determined by sorting the fields into 3-hour bins (00–03

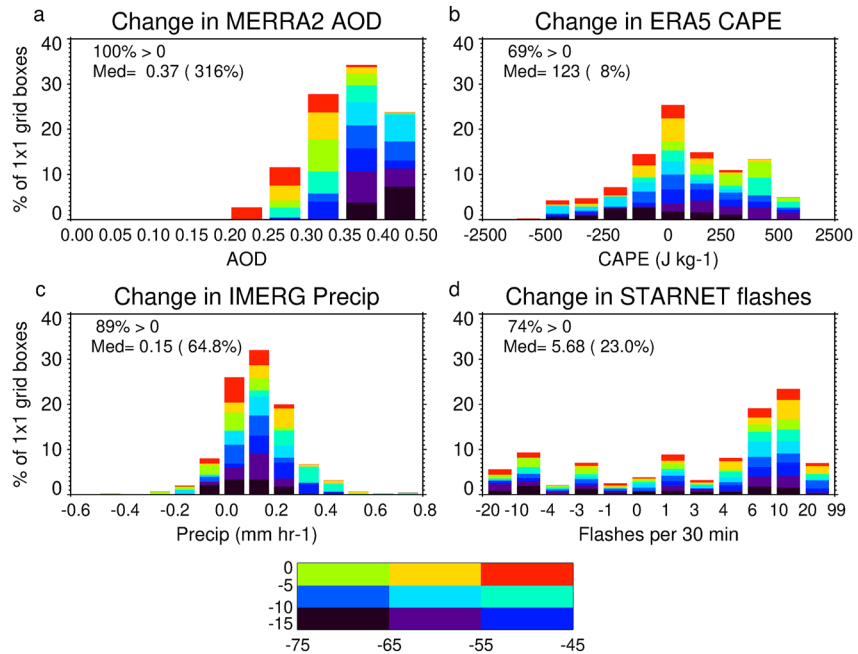


Figure 4. Probability distribution functions showing the percent of the 450 $1^\circ \times 1^\circ$ Amazon Basin grid boxes during August 16–October 15 (pre-monsoon I) of 2012–2017 with changes in Modern-Era Retrospective analysis for Research and Applications-2 aerosol optical depth (AOD) (a), ERA5 convective available potential energy (b), Integrated Multi-satellite Retrievals for Global Precipitation Mission precipitation (c), and Sferics Timing and Ranging Network flashes (d) between the ranges specified on the x axes between clean and dirty 30-min periods. The colors show the contribution of each of the nine 10° in longitude \times 5° in latitude regions to the overall change. The analysis was limited to 30-min periods with rain rates exceeding 0.001 mm hr^{-1} and non-zero flashes. The percent changes are obtained by dividing the median difference of the quantity between the clean and dirty periods by the median value during the clean period. The 30th and 70th percentiles of AOD over the Amazon Basin during these periods (0.15 and 0.29) were used as the thresholds between clean, moderate, and dirty periods (Altaratz et al., 2017).

UTC, 03–06 UTC, etc.) and re-calculating the changes. When this was done, the change in CAPE during the eight periods ranged from 69 to 157 J kg^{-1} (6%–13%), the change in precipitation ranged from 0.08 to 0.16 mm hr^{-1} (59%–108%), and the change in flashes ranged from 2.1 to 8.5 (16%–32%). To test the sensitivity of the results to the method used to determine the aerosol thresholds, the changes were also determined using separate seasonal AOD thresholds for each grid box as opposed to one seasonal threshold for the Basin. When this was done, the median change in AOD was 0.34 (267%), the median change in CAPE was 44 J kg^{-1} (3%), with 56% of the domain having positive changes, the median change in precipitation was 0.13 mm hr^{-1} (54%) with 92% of the grid boxes having positive changes, and the median change in flashes was 4.2 (17%) with 70% of the grid boxes having positive changes. Thus, regardless of how the AOD threshold is specified, precipitation rates were 50%–100% higher and flashes 15%–30% higher during the mid-August to mid-October period when AOD was enhanced. The change in CAPE during this period was relatively modest (3%–13%), suggesting that changes in AOD were responsible for much of the increases in precipitation and flashes.

The sensitivity of precipitation and flashes to aerosol loading was also examined during the latter portion of the pre-monsoon season (October 16–December 15) and found to be less clear. During this period, the median change in AOD was 0.32 (287%), the median change in CAPE was 653 J kg^{-1} (52%), the median change in precipitation was 0.05 mm hr^{-1} (14.3%), and the median change in flashes was 2.1 (8.6%). Thus, during the pre-monsoon-II season, the main difference between the clean and dirty periods was a 52% increase in CAPE, which is certainly large enough to explain the modest increases in precipitation and flashes regardless of the aerosol loading. During this period, changes in precipitation and flashes were relatively modest, and hours with enhanced AOD often also had enhanced CAPE, making it impossible to detect an aerosol signal. The sensitivity of rain- and flash rates to aerosols during pre-monsoon I when the mean value of CAPE was $1,067 \text{ J kg}^{-1}$ but not pre-monsoon II when the mean value was $1,788 \text{ J kg}^{-1}$ (see Figure 3) suggests that convective intensity is more sensitive to aerosol loading when values of CAPE are relatively low.

Table 2
Mean 2012–2017 Rainfall and Flashes During the Pre-Monsoon Period Plus Percentiles of Convective Available Potential Energy and Aerosol Optical Depth Used in Classifying Days as Clean or Dirty

Site	Precip	Flashes	CAPE	CAPE	AOD	AOD
	Daily mean mm 30 min ⁻¹ for 0.9° × 0.9° box that includes site	Daily mean total for the same box	PCTL30 ^a J kg ⁻¹	PCTL70 ^a J kg ⁻¹	PCTL30 ^a Unitless	PCTL70 ^a Unitless
Huancayo-IGP	1.1	56	8	812	0.07	0.12
Rio Branco	2.5	181	795	1,813	0.21	0.45
Ji_Parana_SE	2.4	223	678	2,102	0.24	0.53
Greater Manaus	2.7	264	661	1,641	0.21	0.37
Alta Floresta	3.7	297	639	1,985	0.25	0.51
CUIABA-MIRANDA	1.8	288	169	1,530	0.21	0.47
Brasilia SONDA	3.1	276	2	1,051	0.12	0.23

^aPCTL_{xx} refers to xxth percentiles of ERA-5 CAPE or AERONET AOD at each site.

To further investigate the relationship between CAPE, AOD, precipitation, and flashes, the sensitivity of rain- and flash rates to CAPE and aerosol loading was examined for 0.9° × 0.9° regions centered on the AERONET sites (see Figure 1) using AOD measurements during the pre-monsoon time period. The unusually sized regions were chosen to be similar in size to the 1° × 1° regions used for our earlier analysis and are comprised of 81 0.1° × 0.1° grid boxes with the AERONET site in the middle. The ARM_Manacapuru, Manaus_EMBRAPA, and Amazon_ATTO_Tower sites are located close together and combined into a Greater Manaus data set for analysis. For each of the six actual sites and the Greater Manaus site (see Table 1), AOD measurements taken between 12 and 18 UTC were read in and averaged to obtain representative values for each day. The daily values were then sorted with the highest 30% of the days at each site classified as high-AOD days, the lowest 30% classified as low-AOD days, and the remainder classified as moderate-AOD days (see Table 2). For each site, hourly values of CAPE were then extracted from ERA5 for 12–18 UTC. Maxima of the seven hourly values were then determined for each day with AERONET data, and the maxima were sorted and binned in the same manner as the AOD to define low-CAPE, moderate-CAPE, and high-CAPE days. For each day, the STARNET flashes were summed and IMERG rain-rates were averaged over 0.9° × 0.9° regions centered on 0.1° × 0.1° grid boxes containing the sites to obtain representative values of precipitation and flashes.

Figures 5 and 6 show rain- and flash-rates for each of the nine AOD/CAPE bins. The values were constructed using observations during the pre-monsoon periods of 2012–2017. When controlling for AOD, precipitation increased by a factor of 3.9 between periods with low-and-moderate CAPE and by an additional factor of 1.4 between periods with moderate-and-high CAPE. The mean rain rate on high-CAPE days exceeded the mean rain rate on low-CAPE days by a factor of 5.9 with large regional variations, especially in the eastern Basin, near CUIABA-MIRANDA and Brasilia SONDA, where rain-rates were near zero on low-CAPE days but much higher on high-CAPE days resulting in extremely high ratios (see Table 3). The sensitivity of precipitation to AOD was relatively small with a factor of 2 site-to-site variations in the ratio between high-AOD and low-AOD periods that may be just noise. Specifically, the mean high-AOD to low-AOD precipitation ratio was 0.9, with values ranging from ~0.6 for southwestern sites (Huancayo-IGP, Rio Branco, Ji Parana, and CUAIBA-MIRANDA) to 1–1.3 for the other sites (Table 3). When the ratios were re-calculated using observations from the six-hour period (1500–2059 UT) (HHMM) with the most flashes, the dependence on CAPE increased, and a hint of a weak dependence on aerosol loading emerged. Specifically, the mean ratio of precipitation between high-CAPE and low-CAPE periods increased from 5.9 to 10, while the mean ratio of precipitation between low-AOD and high-AOD periods increased from 0.9 to 1.2.

In the mean, flashes increased by a factor of 7.0 between periods with low-CAPE and periods with high-CAPE with a factor of 4.6 increase between periods with low-and-moderate CAPE and an additional factor of 1.5 increase between periods with moderate-and-high CAPE. When averaged over the three CAPE bins, flashes increased by a factor of 1.3 between periods with low-and-moderate AOD and by an additional 1.6 between periods with moderate-and-high-AOD. The slightly larger percent increase between moderate-and-high AOD loading

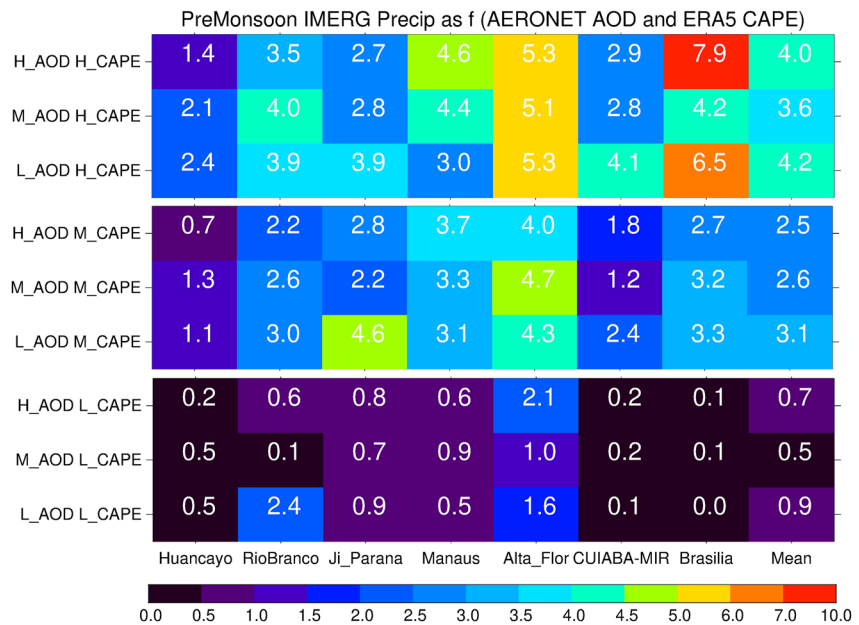


Figure 5. Integrated Multi-satellite Retrievals for Global Precipitation Mission precipitation as a function of convective available potential energy (CAPE) and aerosol optical depth (AOD) at each of the seven Aerosol Robotic Network (AERONET) sites as well as the mean of the seven sites. Site-specific values of the 30th and 70th PCTLs of CAPE over the 12–18 UT period and AERONET AOD over the same period were used to partition days into nine bins containing low-, moderate-, and high values of CAPE and AOD (y-axis). Mean precipitation rates (mm day^{-1} averaged over $0.9^\circ \times 0.9^\circ$ region) for each of these bins are shown for each site as well as the overall mean. The mean ratio of precipitation on high-CAPE days to low-CAPE days was 5.9, while the ratio of precipitation on high-AOD days to low-AOD days was 0.9.

than between low-and-moderate is surprising as several studies show that flash rates tend to level off or decrease with AOD for larger values of AOD; however, the result may not be noise as it is supported by results at four of the sites (Rio Branco, Ji Parana SE, Alta Floresta, and Brasilia) and contradicted by results at only one of the sites

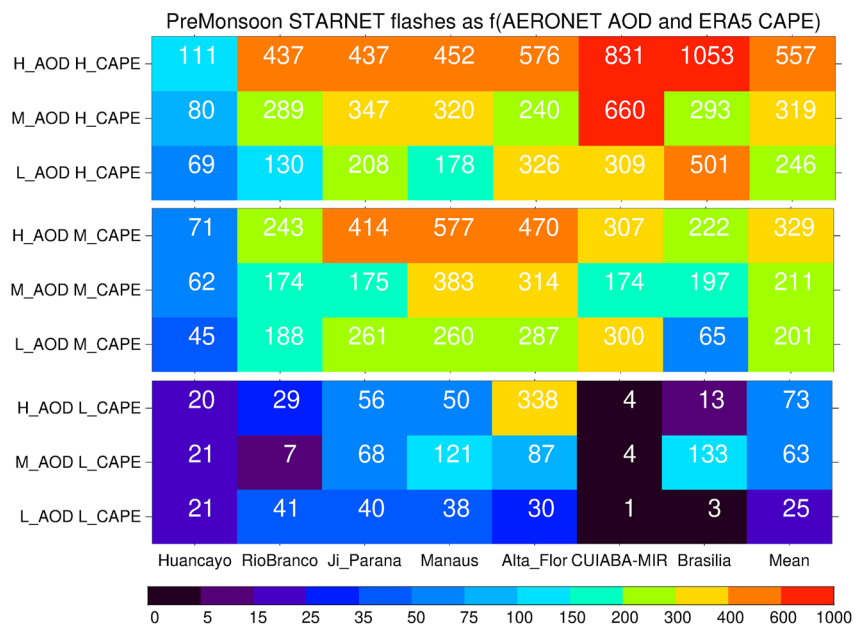


Figure 6. Sferics Timing and Ranging Network flashes for $0.9^\circ \times 0.9^\circ$ regions containing each Aerosol Robotic Network site plus the mean as a function of convective available potential energy and aerosol optical depth using the same bins as Figure 5. The mean ratio of flashes on high-CAPE days to low-CAPE days was 7.0, while the ratio of flashes on high-AOD days to low-AOD days was 2.0.

Table 3
Ratios of Precipitation and Flashes Between Periods With High-CAPE and Low-CAPE and Between Periods With High-AOD and Low-AOD

Site	High CAPE/low CAPE (unstable/stable) ^a		High AOD/low AOD (dirty/clean) ^b	
	Precipitation ratio	Flash ratio	Precipitation ratio	Flash ratio
Huancayo-IGP	5.1	4.3	0.57	1.5
Rio Branco	3.7	11	0.67	2.0
Ji_Parana_SE	3.9	6.1	0.67	1.8
Greater Manaus	6.1	4.6	1.3	2.3
Alta Floresta	3.3	2.5	1.0	2.2
CUIABA-MIRANDA	20.	200	0.72	1.9
Brasilia SONDA	81	12	1.1	2.3
Mean	5.9	7.0	0.89	2.0

^aHigh (Low) CAPE days are days when CAPE exceeds (is less than) the 70th (30th) percentiles given in Table 2. ^bHigh (Low) AOD days are days when AOD exceeds (is less than) the 70th (30th) percentiles given in Table 2.

(Manaus). The mean dependence of flash rate on AOD was largest for low values of CAPE; however, that result is driven by Alta Floresta, where the mean flash rate was a very high 338 flashes per day per $0.9^\circ \times 0.9^\circ$ grid box when AOD and CAPE were high. When that site is excluded, the dependence of flash rate on AOD was actually largest on days with high CAPE. Flash rates on high-AOD days exceeded flash rates on low-AOD days at all seven sites, with the mean ratio equaling 2.0 and local ratios varying modestly from 1.5 at Huancayo-IGP to 2.3 for Greater Manaus and Brasilia SONDA (Table 3). When the ratios were re-calculated using observations from the six-hour period (15–21 UTC) of highest flashes, the ratio of flashes between high-CAPE and low-CAPE days increased from 7.0 to 9.7 while the ratio of flashes between low-AOD and high-AOD days increased from 2.0 to 2.3. Thus, rain- and flash rates increase by a factor of 6–10 between low-CAPE and high-CAPE days. Flash rates are also sensitive to AOD increasing by approximately a factor of 2 at all sites between low-AOD and high-AOD days. However, precipitation response to AOD is mixed with increases more likely during periods and at locations where a relatively high percentage of the rain came from thunderstorms, specifically the eastern portion of the domain and 15–21 UTC.

3.3. Analysis Using MERRA-2 AOD and CloudSat and CALIPSO Profiles

The effects of thermodynamics and microphysics on the vertical structure of deep convective events are now examined using median distributions of Z_e and mean distributions of IWC for deep convective systems sampled by CloudSat and CALIPSO over the Amazon Basin during the pre-monsoon period (see also Chen et al., 2016). As before, representative profiles are obtained after separating the profiles into three instability bins using 30th and 70th percentiles of ERA5 CAPE (990 and 1,959 J kg⁻¹) and three aerosol-loading bins using 30th and 70th percentiles of total column MERRA-2 AOD (0.144 and 0.256). The methods used to obtain representative values of CAPE and AOD for each deep convective system are described in Sections 2.3 and 2.4.

Figure 7 shows the median vertical profiles of Z_e for deep convective systems observed over the Amazon Basin during the pre-monsoon season. The figure contains nine Z_e profiles representing three-levels of instability based on CAPE and three-levels of aerosol loading based on AOD. The mean Z_e for all nine AOD/CAPE bins is ~ 8 dBZ at 7 km. The profiles diverge for altitudes above 7 km due to differences in hydrometeor loading and also because the radar signal in the upper troposphere is less subject to contamination via attenuation and multiple scattering (Protat et al., 2009). The mean Z_e for low-CAPE clean profiles decreases rapidly between 7 and 10 km, while the mean Z_e for high-CAPE dirty profiles increases slightly between 7 and 10 km. Profiles for intermediate levels of CAPE and AOD fall in between the extrema. The different behaviors arise from the sensitivity of the Z_e profile in the mixed phase region to hydrometeor size and phase. Specifically, Z_e is higher for water than for ice and higher for large hydrometeors such as hail or graupel than small hydrometeors. Zipser and Lutz (1994) found that vertical profiles of Z_e for tropical continental storms show a free-troposphere maxima and then decrease gradually with height above the freezing layer. In the mixed phase region, Heiblum et al. (2017) found that Z_e diminished by

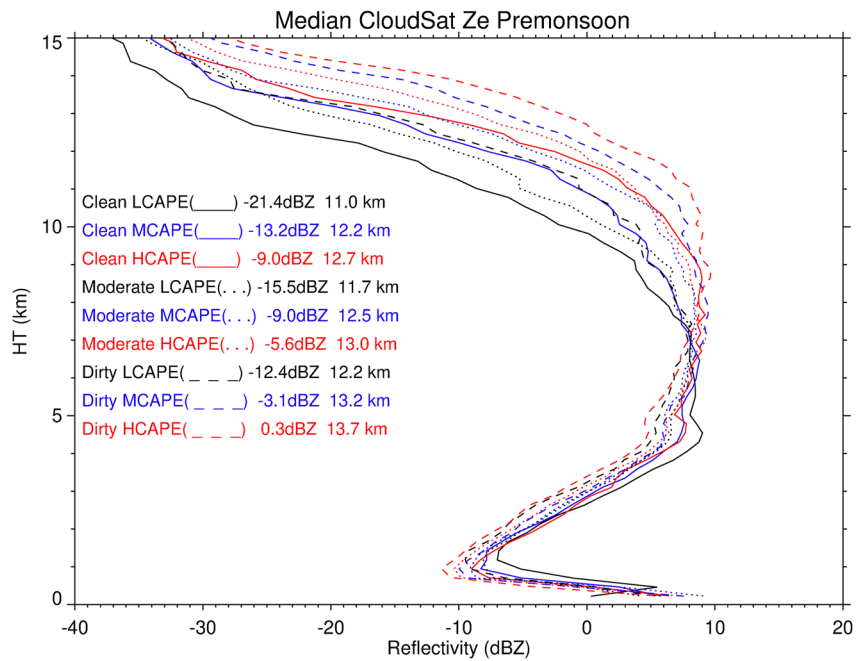


Figure 7. Median vertical profiles of Z_e (dBZ) for deep convective systems over the Amazon Basin during the pre-monsoon time period as a function of ERA5 convective available potential energy (CAPE) and Modern-Era Retrospective analysis for Research and Applications-2 aerosol optical depth (AOD). The bins for CAPE are CAPE <990 J/kg, 990 J/kg < CAPE <1,959 J/kg, and CAPE >1,959 J/kg. The bins for aerosol are AOD <0.144, 0.144 < AOD <0.256, and AOD >0.256. For each of the bins, the mean value of Z_e between 11 and 14 km (e.g., -21.4 dBZ for clean low-CAPE conditions) and the altitude of the -10 dBZ contour (e.g., 13.7 km for dirty high-CAPE conditions) are shown.

3.5–5 dBZ/km over land where aerosols were plentiful. These Z_e profiles show maxima between 5 and 9 km and diminish by 1.3 dBZ/km between 8 and 11 km for dirty high-CAPE profiles to 5.5 dBZ/km between 8 and 11 km for clean low-CAPE profiles. Stolz et al. (2015) showed a “clear, systematic” increase in reflectivity between clean and dirty conditions for shallower and deeper warm cloud depths in all NCAPE environments with largest differences in the mixed phase region.

The mean value of Z_e in the 11–14 km range varied from -21.4 dBZ for clean low-CAPE profiles to 0.3 dBZ for dirty high-CAPE profiles. The altitude of the -10 dBZ contour is usually in this range and varies from 11.0 km for clean low-CAPE profiles to 13.9 km for dirty high-CAPE profiles. Averaging over the AOD bins, the increase in altitude from clean to dirty conditions averages 1.7 km for low values of CAPE and 1.4 km for moderate-and-high values of CAPE. Using the -10 dBZ contour as an estimate of the cloud top height and further assuming that flash rates are proportional to the 4.9th power of cloud top height (Price & Rind, 1992), the 1.4–1.7 km difference in cloud height would correspond to a factor of 1.7–2.0 difference in flash rates between periods with low aerosol-loading and periods with high aerosol loading. Figure 8 shows rain- and flash-rate statistics for convective systems in each of the nine CAPE and AOD bins. These systems were almost always accompanied by rain; however, the percent with lightning varied from 40% for low-CAPE low-AOD conditions to 83% for high-CAPE high-AOD conditions. Summing over the three-CAPE bins, the percentage of systems with flashes increased from 49% for low-AOD conditions to 78% for high-AOD conditions. Similarly, the median rain rate increased from 0.68 to 0.81 mm per 30 min, and the flash count for flashing systems increased from 3.3 to 12.0 flashes per 30 min per $0.3 \times 0.3^\circ$ grid box. The factor of 3.6 increase in flashes is a factor of 2 larger than the expected value of 1.6–2.0 based on the differences in -10 dBZ heights between clean and dirty systems. The mean rain-rate for convective systems with flashes increased from 1.16 to 1.34 mm 30 min^{-1} between the low- and high-AOD bins; a difference that was not significant at the 99% CI. The mean flash rate increased from 14 to 42 flashes per 30 min; a difference that was significant at the 99% CI. This suggests that aerosol loading should also be considered when developing flash rate parameterizations for use in chemical transport and climate models (e.g., Stolz et al., 2017). The relationship between flashes and CAPE is noisier. The percent of deep convective systems with lightning increases with CAPE; however, flash rates of flashing storms were only weakly dependent

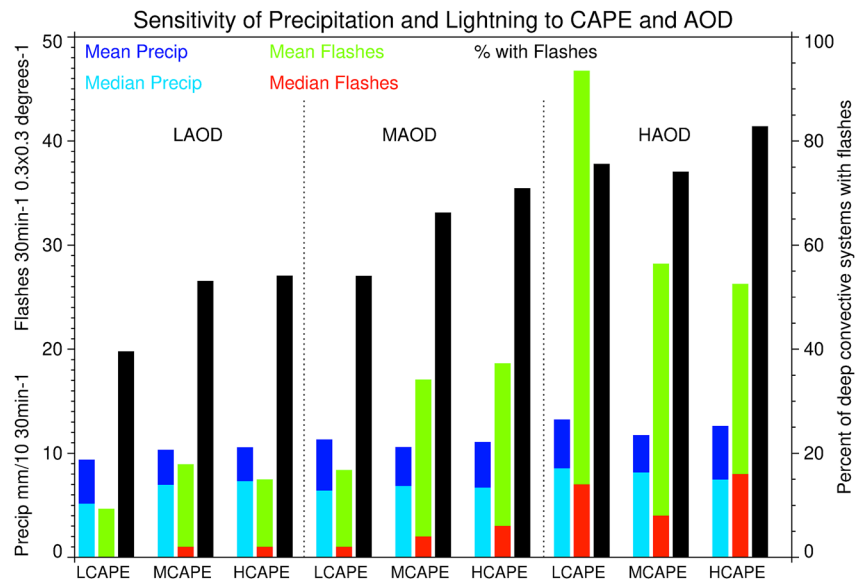


Figure 8. Sensitivity of precipitation and lightning to convective available potential energy (CAPE) and aerosol optical depth (AOD). The left bars in each group of three bars shows the mean and median rain-rates with the mean rate given by the top of the bi-colored bar, the center bars show the mean (top) and median (bottom) flash-rates, and the third bars show the percent of deep convective systems with flashes. Values are shown for low-, moderate-, and high-bins of both CAPE and AOD. Rain-rates are 30-min averages over $0.3^\circ \times 0.3^\circ$ regions centered on convective systems. Flashes are 30-min sums over same regions.

on CAPE. Specifically, flash rates increased with CAPE for low- and moderate-values of AOD but decreased with CAPE for high values of AOD. The surprising results are likely noise, given the volatility of flash rates and the relatively small sample size.

Mean values of Z_e for all combinations of CAPE and AOD decrease with altitude between 11 and 14 km. The rate at which Z_e decreases is associated with the type and concentration of cloud ice particles in the region. Z_e is proportional to the sixth power of hydrometeor size, and large hydrometeors fall out of updrafts more rapidly than smaller hydrometeors (Dodson et al., 2018). Thus, IWC is highly correlated with Z_e (Heymsfield et al., 2016), with dirty high-CAPE profiles containing more ice likely as highly reflective hail or graupel (Dodson et al., 2018) than clean low-CAPE profiles. Mean vertical profiles of IWC for the nine CAPE/AOD bins are shown in Figure 9. After controlling for CAPE, the higher mean values of Z_e and IWC for polluted conditions indicate that polluted storms contain stronger updrafts that are capable of transporting water droplets and hydrometeors to higher altitudes (Chen et al., 2016; Morales-Rodriguez, 2019). The smaller droplet sizes in the polluted storms slow the efficiency of coalescence allowing a higher percentage of the droplets to be lofted into the mixed phase region where glaciation is possible. As expected from the Z_e profiles, mean IWC increases consistently with both CAPE and AOD. For example, between 7 and 15 km, IWC is clearly lowest for clean low-CAPE profiles and clearly highest for dirty high-CAPE profiles. At 10 km, the IWC under low-CAPE conditions equaled 0.30 g m^{-3} for clean conditions and 0.50 g m^{-3} for dirty conditions. Similarly, under moderate-CAPE conditions, IWC equaled 0.45 g m^{-3} and 0.65 g m^{-3} , while under high-CAPE conditions it equaled 0.50 g m^{-3} and 0.73 g m^{-3} . Thus, after controlling for CAPE, IWC increases by 45%–70% between low and high-AOD conditions, with larger increases observed under low-CAPE conditions. The difference in IWC between clean low-CAPE profiles and dirty high-CAPE profiles is \sim a factor of 2.4, with mean IWC equaling 0.35 g m^{-3} for clean low-CAPE profiles and 0.83 g m^{-3} for dirty high-CAPE profiles. Z_{IWC} increases by 1.5 km (18%) between clean low-CAPE profiles and dirty high-CAPE profiles, 1.0 km (12%) between clean and dirty profiles, and 0.4 km (5%) between low- and high-CAPE profiles.

Figure 10 compares the probability distribution functions of Z_{re} , Z_{IWC} , rain rate, and flash rate for deep convective systems sampled under low- and high-aerosol loading. The method used to obtain representative values of Z_{re} and Z_{IWC} for individual convective systems is discussed in Section 2.1. For precipitation, the values shown are the means over the Amazon Basin of rain rates during the 30-min period that contains the overpass. For

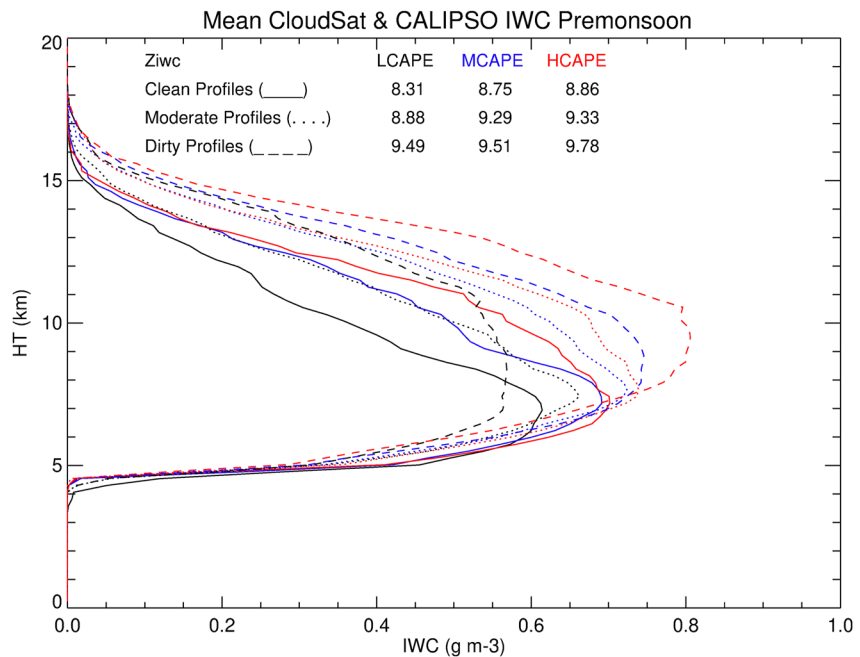


Figure 9. Mean vertical profiles of ice water content for deep convective systems over the Amazon Basin during the pre-monsoon season with the same convective available potential energy and aerosol optical depth bins as in Figure 7. For each of the nine bins, the altitude of the Z_{IWC} centroid is shown.

flashes, the values shown are the means over the Amazon Basin of three ten-minute periods chosen so that the time of the overpass is in the middle period. The mean Z_{re} increases 1.3 km between periods with low- and high-AOD, a difference that is significant at the 99% confidence level (CL). Similarly, the mean Z_{IWC} increases by 1.0 km, a difference that is also significant at the 99% CL. The mean rain-rate increased by 14% between low- and high-AOD conditions, an increase that was not significant at the 95% CL due to the high variability in precipitation rates. Finally, the mean flash rate increased by \sim a factor of 5, an increase that is significant at the 99% CL despite the high variability in flash rates. Statistically significant differences in Z_{re} , Z_{IWC} , and flash rate between clean and dirty periods were observed during both the pre-monsoon I and pre-monsoon II portions of the pre-monsoon period. However, the contrast in flashes between clean and dirty periods was roughly a factor of 10 during pre-monsoon I but only a factor of 3 during pre-monsoon II. The different responses could be caused by differences in WCD between the periods. In pre-monsoon I, the mean WCD was 4.00 km for clean systems and 3.93 km for dirty systems. In pre-monsoon II, the mean WCD was 3.92 km for clean systems and 4.12 km for dirty systems. Thus, during pre-monsoon I, differences in WCD are responsible for a small portion of the increase in flashes between clean and dirty conditions. While, during pre-monsoon II, the larger WCD during dirty periods partially offsets the role of enhanced aerosols and lessens the effect (see Stolz et al., 2015).

Q. Wang et al. (2018) found that flash rates in smoke-dominant regions of Africa were greater than in dust-dominated regions primarily because mid-level RH was 74% in the smoke-dominant region and only 36% in the dust-dominant region. However, in this study, the mean RH in the mid-troposphere over the Amazon Basin was 74% for clean convective systems with fewer flashes and 65% for dirty convective systems with more flashes. The median lower troposphere static stability, that is, the change in potential temperature between the surface and 700 hPa, was -12.1 K for clean systems and -11.9 K for dirty systems. Thus, the potential temperature increased slightly more rapidly with height when systems were dirty, indicating a similar or possibly slightly less stable environment. Thus, while the dirty profiles tended to have drier air in the mid-troposphere, which is a barrier to weak convection (Wall et al., 2014), the associated steeper lapse rates may have made the atmosphere more conducive to intense convection once the convective inhibition was overcome.

To control for variations in thermodynamic forcing with AOD, we also examined variations in the centroid of Z_e (Z_{re}), and IWC (Z_{IWC}), precipitation rate, and flash rate with AOD after binning each variable into low-, moderate-, and high-CAPE bins (see Table 4). Increases in Z_{re} , Z_{IWC} , rain-rate, and flash-rate were still observed

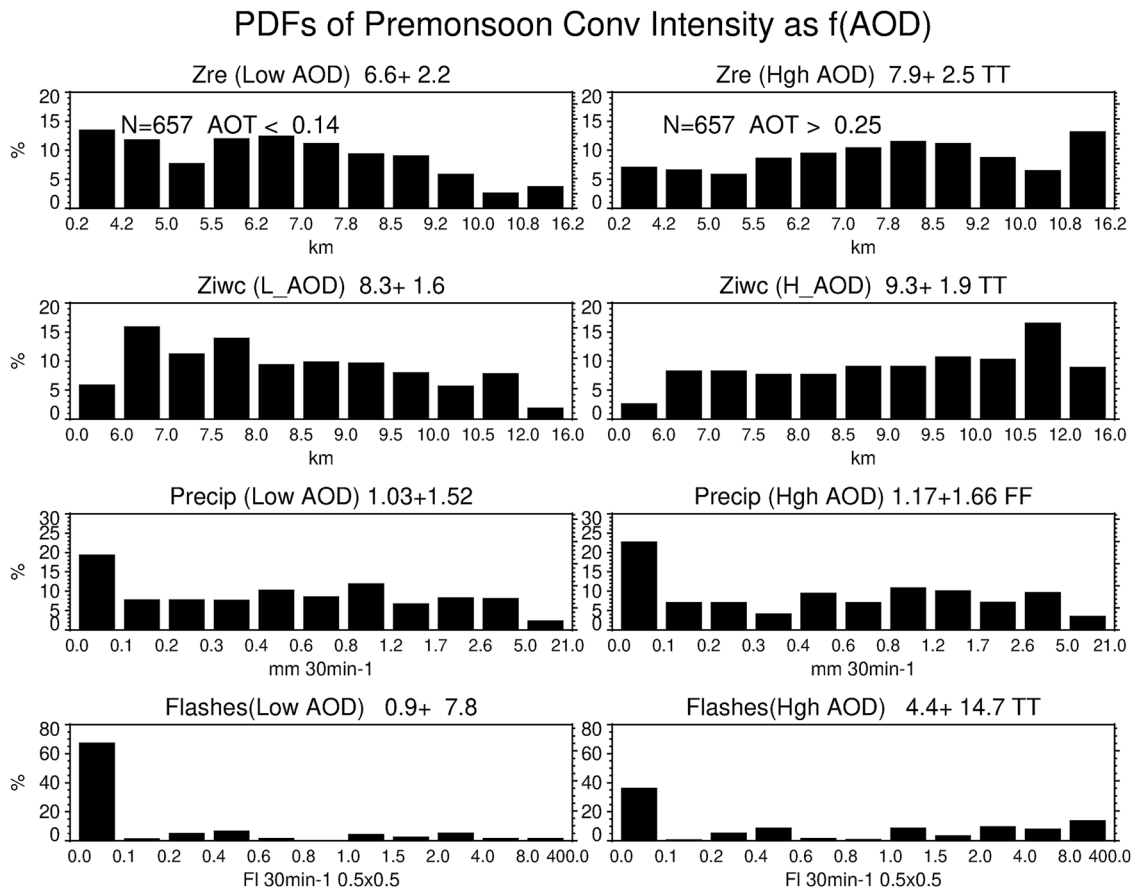


Figure 10. Probability distribution functions of centroid of radar reflectivity (Z_{re} , top row), centroid of ice water content (Z_{iwc} , second row), rain rate (third row), and flash rate (bottom row) for pre-monsoon profiles sampled under low-aerosol loading (Modern-Era Retrospective analysis for Research and Applications-2 aerosol optical depth (AOD) < 0.14) (left column) and high-aerosol loading (AOD > 0.26) (right column). Mean and standard deviation are shown for each variable. TT indicates that the difference is significant at the 99% confidence level (CL), while FF indicates that the difference is insignificant at the 95% CL.

Table 4
Sensitivity of Convective Metrics to Aerosol Optical Depth After Controlling for Convective Available Potential Energy

	Low AOD (<30th PCTL)	High AOD (>70th PCTL)	Significant difference at 99% CL?	Significant difference at 95% CL?
Z_{re} Low CAPE ^a	6.1 ± 2.1 (240) ^b	7.6 ± 2.6 (164)	Yes	Yes
Z_{re} Moderate CAPE	6.7 ± 2.2 (241)	6.9 ± 2.1 (251)	No	No
Z_{re} High CAPE	7.2 ± 2.2 (133)	8.4 ± 2.5 (198)	Yes	Yes
Z_{iwc} Low CAPE	7.9 ± 1.6	9.1 ± 2.0	Yes	Yes
Z_{iwc} Moderate CAPE	8.5 ± 1.6	9.4 ± 1.8	Yes	Yes
Z_{iwc} High CAPE	8.8 ± 1.6	9.7 ± 1.9	Yes	Yes
Precip Low CAPE	0.92 ± 1.27	1.2 ± 1.7	No	No
Precip Moderate CAPE	1.1 ± 1.6	1.1 ± 1.5	No	No
Precip High CAPE	1.2 ± 1.5	1.3 ± 1.9	No	No
Flashes Low CAPE	0.59 ± 2.0	7.0 ± 26	Yes	Yes
Flashes Moderate CAPE	1.5 ± 13	3.5 ± 8.4	No	Yes
Flashes High CAPE	0.84 ± 2.0	3.7 ± 7.1	Yes	Yes

^aUnits for Z_{re} , Z_{iwc} , precipitation, and flashes are km, km, mm 30 min⁻¹, and flashes per $0.5^\circ \times 0.5^\circ$ grid box per 30-min. ^bNumber of cases in each CAPE/AOD bin.

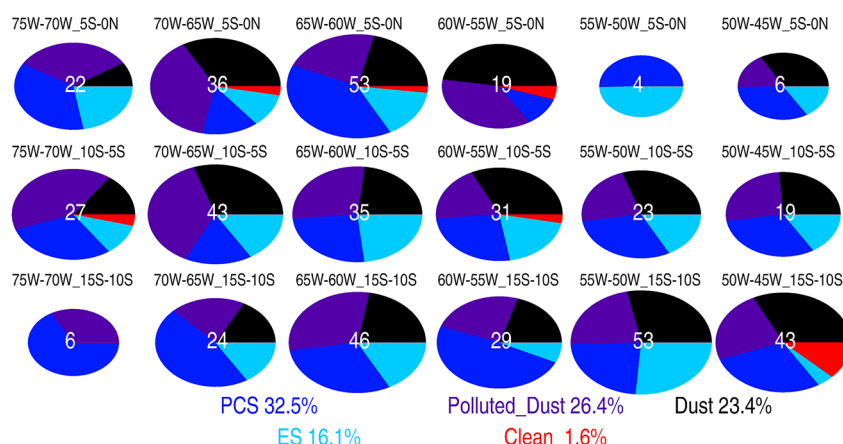


Figure 11. Pie charts showing regional variations in distribution of CALIOP aerosol types for deep convective systems observed during the pre-monsoon season. The number of systems for which typing was possible is shown in the center of each pie. The percent of the systems of each type is shown at the bottom. The “Clean” aerosol type is a summation of Clean Continental and Clean Marine. To emphasize regional differences in the number of convective systems while maintaining readability, the radius of the pies varies with the number of observations divided by the maximum number of observations (53) to the power 0.2.

in all CAPE bins. As before, precipitation increased with AOD ($0.08\text{--}0.30\text{ mm }30\text{ min}^{-1}$), but the increases were not significant at the 95% CL. Increases in Z_{re} were significant for low- and high-CAPE bins but insignificant at the 95% CL for moderate levels of CAPE. Notably, the flash rate under low-CAPE conditions increased from 0.59 ± 2.0 flashes per $0.5^\circ \times 0.5^\circ$ grid box per 30-min under low aerosol conditions to 7.0 ± 26 flashes per $0.5^\circ \times 0.5^\circ$ grid box per 30-min under high-aerosol conditions (an increase by a factor of 12). Thus, convective development and electrification appear to be especially sensitive to aerosol loading during periods with relatively low values of CAPE. That said, flash rates still increased by a factor of 2–4 between periods with low- and high-AOD when CAPE was moderate or high.

3.4. Sensitivity of Flash Rate to Aerosol Type

Prior studies have shown that the intensity of deep convective storms can be sensitive to aerosol type (Jiang et al., 2018; Yang et al., 2016). However, the effect of aerosol type on the intensity of deep convection is complex. When smoke is dominant, that is, δ_p is relatively small, the fine mode is dominant, and particles are mainly spherical, relatively small, and moderately absorbing. Yang et al. observed that the frequency, height, and flash rate associated with thunderstorms peaked on the weekend over central China, where aerosol absorption was strong, suppressing mid-week storms. But the peak occurred on weekdays over southeastern China where the aerosol single scattering albedo was much higher, lessening the aerosol radiative effect, and conditions were more humid, enhancing convective invigoration through the aerosol microphysical effect. Q. Wang et al. (2018) found that flash rates in smoke-dominant regions of Africa were greater than in dust-dominated regions primarily because mid-level RH was greater in the smoke-dominant region; however, aerosol type may also have played a role. Smoke aerosols are likely to absorb more than dust particles. While this absorption inhibits convection by decreasing the amount of radiation reaching the surface, it could also increase the intensity of convection as heating the aerosols layer destabilizes layers above the aerosol layer (Y. Wang et al., 2013).

To follow-up on these studies, we analyzed the lower tropospheric CALIOP aerosol type for the 1,803 convective systems that occurred during the pre-monsoon season (see Section 2.2). The aerosol type was identified for 519 systems, with 132, 144, 152, 81, and 10 systems identified as Dust, Polluted Dust, PCS, ES, and Clean (either Clean Continental or Clean Marine). The spatial distribution of the aerosol types for the systems is shown in Figure 11. Statistics for the systems classified as Dust, Polluted Dust, PCS, and ES are shown in Table 5. The sampled systems cover most of the Domain, suggesting that the statistics should be representative of a variety of environments despite regional variations in the frequency of convection and loss of data due to low-energy shots. Overall, the most common CALIOP aerosol type was PCS (152 cases; 32.5%), followed closely by Polluted Dust (26.4%) and Dust (23.4%). ES in the “lower troposphere” was also relatively common (16.1%) although the

Table 5
Sensitivity of Environmental and Convective Intensity Variables to Dominant CALIOP Aerosol Type in the Lower Troposphere ($P > 675$ hPa)

Variable	Units	Dust	Poll D	Poll C Smk	Elev Smk
# of Cases	Count	132	144	152	81
AOD	Unitless	0.221	0.275	0.251	0.358
CAPE	J kg ⁻¹	1,508	1,766	1,540	1,822
Mid-RH	%	68.4	61.5	62.6	61.0
Z _{TWC}	km	8.56	8.85	9.06	9.17
Precip	mm 30 min ⁻¹	0.74	0.80	1.20	1.39
Flashes	Count 30 min ⁻¹ 0.1° × 0.1° box ⁻¹	1.16	2.47	4.79	3.54

statistics for ES over-represent the southeast, specifically, 10–15°S and 55–50°W, where nearly 30% of the ES events occurred.

In the mean, flash rates were 2–4 × higher when PCS or ES was the most common CALIOP aerosol type as opposed to Dust or Polluted Dust (PD). However, these differences were not significant at the 99% CL due to the limited sample and large variability of flashes. The mean flash rate when dust was dominant was statistically less than the flash rates for the other categories at the 95% CL. Similarly, precipitation-rates were 50%–90% greater when PCS or ES was the most common type as opposed to Dust or PD. The mean precipitation rates when Dust or PD was most common were statistically less than the precipitation rates when PCS (95% CL) or ES (99% CL) was most common. The cause of the weaker storms when dust was present is likely due to the relatively low values of CAPE, AOD and relatively high value of mid-tropospheric RH. This combination is often associated with less intense convection but not necessarily less rain. However, aerosol type may also have played a role because pristine dust is a less efficient CCN and more efficient IN than smoke due to its low solubility and relatively large size (Murray et al., 2012). However, the situation is complex because the efficacy of dust as a CCN increases with time as dust particles are coated by hygroscopic aerosol species during aging. The periods when Polluted Dust was most common had moderate values of AOD, relatively high CAPE, and fairly low mid-tropospheric RH. Precipitation-rates were similar to the Dusty period, but the systems were more intense with higher values of Z_{TWC} and flash rate. The PCS period had moderate values of AOD and CAPE but surprisingly intense convection with high values of Z_{TWC}, precipitation, and flashes. Interestingly, these results are consistent with Jiang et al. (2018), who observed higher values of Z_{TWC} over the Amazon under PCS-conditions as opposed to aerosol-free conditions. Finally, the “ES” period featured high mean values of CAPE and AOD. The ES may contribute to the larger rain- and flash-rates via changes to ice nucleation properties (e.g., Jahl et al., 2021), but it may also be a consequence of additional lofting associated with higher-than-average values of CAPE.

4. Conclusions

In this study, the sensitivity of rain- and flash rates to instability and aerosol amount were examined over the Amazon Basin during the pre-monsoon season (August 16–December 15) using metrics of convective intensity over deep convective scenes derived from CloudSat, total column AOD from AERONET and MERRA-2, aerosol types from CALIPSO, precipitation fields from IMERG, and flash rates from STARNET. The pre-monsoon season was chosen because it is a period with large variations in aerosols and the highest percentage of lightning-producing deep convective systems.

Initially, changes in CAPE, rain rate, and lightning flashes were examined as a function of aerosol loading using hourly time series of MERRA-2 AOD, ERA5 CAPE, IMERG precipitation, and STARNET flashes during the pre-monsoon I (August 16–October 15) and pre-monsoon II (October 16–December 15) time periods. During pre-monsoon I, precipitation rates were 50%–100% higher and flashes 15%–30% higher during hours with high-AOD than in hours with low AOD. The change in CAPE during this period was relatively modest, suggesting that changes in AOD were responsible for much of the increases in precipitation and flashes. The sensitivity of flashes to aerosol loading was less clear during pre-monsoon II possibly because enhancements due to aerosols were offset by reductions in the intensity of convection due to larger values of WCD. During this period, changes

in precipitation and flashes were small, and hours with enhanced AOD often also had enhanced CAPE, making it impossible to detect an aerosol signal. The sensitivity of rain- and flash-rates to aerosols during pre-monsoon I when CAPE is relatively low but not pre-monsoon II when CAPE is often high suggests that convective intensity may be more sensitive to aerosol loading when values of CAPE and WCD are relatively low.

The relationship between convective intensity and aerosol loading was then examined using AERONET AOD as a metric for aerosol loading and rain- and flash-rates for regions encompassing the AERONET sites. Both rain- and flash-rates increased by a factor of 5–10 between low-CAPE and high-CAPE days. Flash rates were also sensitive to AOD, increasing by approximately a factor of 2 at all sites between low-AOD and high-AOD days. The dependence of precipitation on AOD was more complex, but a weak positive relationship was found for times and regions when convective storms were common, specifically for afternoon hours and the eastern portion of the Basin.

Vertical profiles of radar reflectivity (Z_e) and IWC from CloudSat and CALIPSO were then used to examine the effects of thermodynamic and microphysical forcing on the structure of deep convective events. The values of Z_e diverged between 7 and 10 km, with Z_e decreasing rapidly for clean low-CAPE profiles but remaining steady for dirty high-CAPE profiles. This indicates that the vertical velocities in dirty-high CAPE environments were large enough to sustain a high concentration of larger hydrometeors, while vertical velocities in clean low-CAPE environments were insufficient to sustain high concentrations of larger hydrometeors. The cloud top altitude was ~3 km higher for dirty high-CAPE storms than for clean low-CAPE storms. Controlling for CAPE, flash rates increased by more than a factor of 3 between clean and dirty periods, about twice as much as expected, given observed differences in convective cloud top heights. This suggests that aerosol loading should also be considered when developing flash rate parameterizations for use in chemical transport models and climate models. IWC increased by a factor of 2.4 between clean low-CAPE profiles and dirty high-CAPE profiles. Controlling for CAPE, IWC increased by 50%–60%, and Z_{TWC} increased by 1.0 km between clean and dirty conditions.

The statistical significances of contrasts in Z_{re} , Z_{TWC} , rain-rate, and flash-rate between deep convective systems sampled under low- and high-aerosol loading were then examined. Z_{re} and Z_{TWC} increased by 1.4 and 1.1 km, respectively, differences that were significant at the 99% CL. The rain-rate increased by a modest 17%, an increase that was not significant at the 95% CI, while flash rates increased by 450%, an increase that was significant at the 99% CL. Thus, when individual convective systems were examined, as opposed to larger regions, for example, $1^\circ \times 1^\circ$, the response of rain-rates to increasing AOD was muted, possibly because focusing on an individual system emphasizes decreases in rain rate that may occur under high aerosol loading because droplets are too small to be rained out and are lofted into the mixed phase region. The contrast in mid-tropospheric RH and LTSS between clean and dirty periods was also examined. In general, the RH was lower in dirty systems, while the LTSS was slightly larger. The lower RH and associated steeper lapse rates for dirty systems appear to make the atmosphere more conducive to intense convection and reinforce the large role thermodynamic forcing plays in determining the intensity of convection.

The sensitivity of flashes to the composition of aerosols was also examined. The most common CALIOP aerosol types associated with the deep convective systems observed in this study were PCS (33%), Polluted Dust (26%), Dust (23%), and ES (16%). Overall, the flash rate was 2–4 × greater when ES or PCS (i.e., smoke) was the main CALIOP aerosol type in the lower troposphere as opposed to Dust or Polluted Dust. The flash rates when smoke was present are likely higher because these periods also had higher values of CAPE and AOD and lower values of mid-tropospheric RH. However, it is also possible that the smoke particles may act as ice nuclei or affect the stability through absorption and heating. Thus, aerosol type may also play a role in explaining the differences.

Data Availability Statement

The 2B-GEOPROF (Marchand et al., 2008), 2B-CLDCLASS (Sassen & Wang, 2008), and 2C-ICE (Deng et al., 2015) data sets were acquired via sftp from the CloudSat Data Processing Center (<https://www.cloudsat.cira.colostate.edu/>). CALIPSO data (Kim et al., 2018) were acquired from the NASA EARTHDATA site (<https://asdc.larc.nasa.gov/data/CALIPSO/>). MERRA-2 AOD (GMAO, 2015) were accessed from https://gmao.gsfc.nasa.gov/reanalysis/MERRA-2/data_access/. ERA5 CAPE (Hersbach et al., 2020) is available as part of the “ERA5 hourly data on single levels from 1940 to present” collection accessible at <https://cds.climate.copernicus.eu/cdsapp#!/dataset/reanalysis-era5-single-levels?tab=form>. Level 2 Spectral Deconvolution Algorithm (SDA)

retrievals of AERONET AOD data for the Amazon Basin (Palacios et al., 2022) were obtained at <https://aeronet.gsfc.nasa.gov/>. IMERG precipitation data (Huffman et al., 2014) were accessed from the Goddard Earth Sciences Data and Information Center (GES DISC) at https://disc.gsfc.nasa.gov/datasets/GPM_3IMERGHH_06/summary?keywords=%22IMERG%20final%22. STARNET data (Morales-Rodriguez et al., 2014) for the Amazon Basin were obtained from co-author Morales-Rodriguez.

The data sets and software needed to generate the plots and figures in the manuscript are archived on the Digital Repository at the University of Maryland (DRUM) at <http://hdl.handle.net/1903/30416>. The research products archived in DRUM will be available indefinitely. The University of Maryland Libraries' DRUM repository is built on DSpace software, a widely used, reliable digital repository platform. DRUM performs nightly bit-level integrity tests on all files, and all contents are regularly copied to back-up storage. DRUM conforms to the digital preservation principles outlined in the University of Maryland Libraries' Digital Preservation Policy.

Acknowledgments

The authors acknowledge the support of NASA Grant 80NSSC20K0131 that was awarded to first author Dale Allen under the NASA ROSES-2018 CloudSat and CALIPSO solicitation. Ken Pickering, Siyu Shan, and Melody Avery were also supported under this Grant. Z. Li was supported by the National Science Foundation (AGS2126098). In addition, co-author P. Artaxo acknowledges funding from FAPESP through Grant 2017/17047-0.

References

- Albrecht, R. I., Morales, C. A., & Silva-Dias, M. A. F. (2011). Electrification of precipitating systems over the Amazon: Physical processes of thunderstorm development. *Journal of Geophysical Research*, *116*(D8), D08209. <https://doi.org/10.1029/2010JD014756>
- Altartaz, O., Koren, I., Yair, Y., & Price, C. (2010). Lightning response to smoke from Amazonian fires. *Geophysical Research Letters*, *37*(7). <https://doi.org/10.1029/2010GL042679>
- Altartaz, O., Kucienska, B., Kostinski, A., Raga, G. B., & Koren, I. (2017). Global association of aerosol with flash density of intense lightning. *Environmental Research Letters*, *12*(11), 114037. <https://doi.org/10.1088/1748-9326/aa922b>
- Andreae, M. O., Acevedo, O. C., Araújo, A., Artaxo, P., Barbosa, C. G. G., Barbosa, H. M. J., et al. (2015). The Amazon Tall Tower Observatory (ATTO): Overview of pilot measurements on ecosystem ecology, meteorology, trace gases, and aerosols. *Atmospheric Chemistry and Physics*, *15*(18), 10723–10776. <https://doi.org/10.5194/acp-15-10723-2015>
- Andreae, M. O., Rosenfeld, D., Artaxo, P., Costa, A. A., Frank, G. P., Longo, K. M., & Silva-Dias, M. A. F. (2004). Smoking rain clouds over the Amazon. *Science*, *303*(5662), 1337–1342. <https://doi.org/10.1126/science.1092779>
- Artaxo, P., Hansson, H.-C., Andreae, M. O., Bäck, J., Alves, E. G., Barbosa, H. M. J., et al. (2022). Tropical and boreal forest – Atmosphere interactions: A review. *Tellus B: Chemical and Physical Meteorology*, *74*(1), 24–163. <https://doi.org/10.16993/tellusb.34>
- Artaxo, P., Vanderlei-Martins, J., Yamasoe, M. A., Procópio, A. S., Pauliquevis, T. M., Andreae, M. O., et al. (2002). Physical and chemical properties of aerosols in the wet and dry seasons in Rondônia, Amazonia. *Journal of Geophysical Research*, *107*(D20). <https://doi.org/10.1029/2001JD000666>
- Blyth, A. M., Christian, H. J., Driscoll, K., Gadian, A. M., & Latham, J. (2001). Determination of ice precipitation rates and thunderstorm anvil ice contents from satellite observations of lightning. *Atmospheric Research*, *59–60*, 217–229. [https://doi.org/10.1016/S0169-8095\(01\)00117-X](https://doi.org/10.1016/S0169-8095(01)00117-X)
- Buchard, V., Randles, C. A., da Silva, A. M., Darnenov, A., Colarco, P. R., Govindaraju, R., et al. (2017). The MERRA-2 aerosol reanalysis, 1980 – Onward, Part 2: Evaluation and case studies. *Journal of Climate*. <https://doi.org/10.1175/JCLI-D-16-0613.1>
- Buiat, M., Porcù, F., & Dietrich, S. (2017). Observing relationships between lightning and cloud profiles by means of a satellite-borne cloud radar. *Atmospheric Measurement Techniques*, *10*(1), 221–230. <https://doi.org/10.5194/amt-10-221-2017>
- Chen, T., Guo, J., Li, Z., Zhao, C., Liu, H., Cribb, M., et al. (2016). A CloudSat perspective on the cloud climatology and its association with aerosol perturbations in the vertical over eastern China. *Journal of the Atmospheric Sciences*, *73*(9), 3599–3616. <https://doi.org/10.1175/JAS-D-15-0309.1>
- Chin, M., Ginoux, P., Kinne, S., Torres, O., Holben, B. N., Duncan, B. N., et al. (2002). Tropical aerosol optical thickness from the GOCART model and comparisons with satellite and sun photometer measurements. *Journal of the Atmospheric Sciences*, *59*(3), 461–483. [https://doi.org/10.1175/1520-0469\(2002\)059<0461:TAOTFT>2.0.CO;2](https://doi.org/10.1175/1520-0469(2002)059<0461:TAOTFT>2.0.CO;2)
- Choi, Y., Wang, Y., Zeng, T., Martin, R. V., Kurosu, T. P., & Chance, K. (2005). Evidence of lightning NO_x and convective transport of pollutants in satellite observations over North America. *Geophysical Research Letters*, *32*(2), L02805. <https://doi.org/10.1029/2004GL021436>
- Cronk, H., & Partain, P. (2017). CloudSat ECMWF-AUX auxiliary data product description and interface control document [Dataset]. https://www.cloudsat.cira.colostate.edu/cloudsat-static/info/dl/ecmwf-aux/ECMWF-AUX_PDICD.P_R05.rev0_.pdf
- Cummins, K. L., Murphy, M. J., Bardo, E. A., Hiscox, W. L., Pyle, R. B., & Pifer, A. E. (1998). A combined TOA/MDF technology upgrade of the US national lightning detection network. *Journal of Geophysical Research*, *103*(D8), 9035–9044. <https://doi.org/10.1029/98JD00153>
- Deng, M., Mace, G. G., Wang, Z. E., & Berry, E. (2015). CloudSat 2C-ICE product update with a new Z(e) parameterization in lidar-only region [Dataset]. *Journal of Geophysical Research*, *120*(23). <https://doi.org/10.1002/2015JD023600>
- Deng, M., Mace, G. G., Wang, Z. E., & Lawson, R. P. (2013). Evaluation of several A-Train ice cloud retrieval products with in situ measurements collected during the SPARTICUS campaign. *Journal of Applied Meteorology and Climatology*, *52*(4), 1014–1030. <https://doi.org/10.1175/JAMC-D-12-054.1>
- Dodson, J. B., Taylor, P. C., & Branson, M. (2018). Microphysical variability of Amazonian deep convective cores observed by CloudSat and simulated by a multi-scale modeling framework. *Atmospheric Chemistry and Physics*, *18*(9), 6493–6510. <https://doi.org/10.5194/acp-18-6493-2018>
- Estevan, R., Martínez-Castro, D., Suarez-Salas, L., Moya, A., & Silva, Y. (2019). First two and a half years of aerosol measurements with an AERONET sunphotometer at the Huancayo Observatory, Peru. *Atmospheric Environment*, *X*(3), 100037. <https://doi.org/10.1016/j.aeaoa.2019.100037>
- Fan, J., & Li, Z. (2022). Aerosol interaction with deep convection. *Aerosols and Climate*, 571–617. <https://doi.org/10.1016/B978-0-12-819766-0.00001-8>
- Fan, J., Rosenfeld, D., Zhang, Y., Giangrande, S. E., Li, Z., Machado, L. A., et al. (2018). Substantial convection and precipitation enhancement by ultrafine aerosol particles. *Science*, *359*(6374), 411–418. <https://doi.org/10.1126/science.aan8461>
- Fan, J., Wang, Y., Rosenfeld, D., & Liu, X. (2016). Review of aerosol–cloud interactions: Mechanisms, significance, and challenges. *Journal of the Atmospheric Sciences*, *73*(11), 4221–4252. <https://doi.org/10.1175/jas-d-16-0037.1>
- Fan, J., Yuan, T., Comstock, J. M., Ghan, S., Khain, A., Leung, L. R., et al. (2009). Dominant role by vertical wind shear in regulating aerosol effects on deep convective clouds. *Journal of Geophysical Research*, *114*(D22), D22206. <https://doi.org/10.1029/2009JD012352>

- Freud, E., & Rosenfeld, D. (2012). Linear relation between convective cloud drop number concentration and depth for rain initiation. *Journal of Geophysical Research*, *117*(D2), D02207. <https://doi.org/10.1029/2011JD016457>
- Freud, E., Rosenfeld, D., & Kulkarni, J. R. (2011). Resolving both entrainment-mixing and number of activated CCN in deep convective clouds. *Atmospheric Chemistry and Physics*, *11*(24), 12887–12900. <https://doi.org/10.5194/acp-11-12887-2011>
- Gelaro, R., McCarty, W., Suárez, M. J., Todling, R., Molod, A., Takacs, L., et al. (2017). The modern-era retrospective analysis for research and applications, version 2 (MERRA-2). *Journal of Climate*, *30*(14), 5419–5454. <https://doi.org/10.1175/jcli-d-16-0758.1>
- Global Modeling and Assimilation Office (GMAO). (2015). MERRA-2 tavg1_2d_aer_Nx: 2d,1-Hourly,Time-averaged, single-level, assimilation, aerosol diagnostics V5.12.4, greenbelt, MD, USA, Goddard Earth Sciences data and information services center (GES DISC) [Dataset]. <https://doi.org/10.5067/KLICLTZ8EM9D>
- Grabowski, W. W., & Morrison, H. (2020). Do ultrafine cloud condensation nuclei invigorate deep convection. *Journal of the Atmospheric Sciences*, *77*(7), 2567–2583. <https://doi.org/10.1175/JAS-D-20-0012.1>
- Guo, J., Deng, M., Lee, S. S., Wang, F., Li, Z., Zhai, P., et al. (2016). Delaying precipitation and lightning by air pollution over the pearl river delta, Part I: Observational analyses. *Journal of Geophysical Research: Atmospheres*, *121*(11), 6472–6488. <https://doi.org/10.1002/2015JD023257>
- Heiblum, R., Koren, I., & Altaratz, O. (2012). New evidence of cloud invigoration from TRMM measurements of rain center of gravity. *Geophysical Research Letters*, *39*(8), L08803. <https://doi.org/10.1029/2012GL051158>
- Heiblum, R. H., Koren, I., Altaratz, O., & Kostinski, A. B. (2017). The consistent behavior of tropical rain: Average reflectivity vertical profiles determined by rain top height. *Journal of Hydrometeorology*, *18*(3), 591–609. <https://doi.org/10.1175/jhm-d-16-0078.1>
- Hersbach, H., Bell, B., Berrisford, P., Hirahara, S., Horányi, A., Muñoz-Sabater, J., et al. (2020). The ERA5 global reanalysis [Dataset]. *Quarterly Journal of the Royal Meteorological Society*, *146*(730), 1999–2049. <https://doi.org/10.1002/qj.3803>
- Heymsfield, A. J., Matrosov, S. Y., & Wood, N. B. (2016). Toward improving ice water content and snow-rate retrievals from radars. Part I: X and W bands, emphasizing CloudSat. *Journal of Applied Meteorology and Climatology*, *55*(9), 2063–2090. <https://doi.org/10.1175/JAMC-D-15-0290.1>
- Holben, B. N., Tanré, D., Smirnov, A., Eck, T., Slutsker, I., Auhassan, N., et al. (2001). An emerging ground-based aerosol climatology: Aerosol optical depth from AERONET. *Journal of Geophysical Research*, *106*(D11), 12067–12097. <https://doi.org/10.1029/2001JD900014>
- Hollingsworth, A., Engelen, R. J., Textor, C., Benedetti, A., Boucher, O., Chevallier, F., et al. (2008). Toward a monitoring and forecasting system for atmospheric composition. *Bulletin of the American Meteorological Society*, *89*(8), 1147–1164. <https://doi.org/10.1175/2008bams2355.1>
- Huffman, G., Bolvin, D., Braithwaite, D., Hsu, K., Joyce, R., & Xie, P. (2014). Integrated multi-satellite retrievals for GPM (IMERG), version 4.4. NASA's precipitation processing center [Dataset]. <https://gpm.nasa.gov/data>
- Huffman, G. J., Bolvin, D. T., Braithwaite, D., Hsu, K., Joyce, R., Kidd, C., et al. (2019). *Algorithm theoretical basis document (ATBD) version 5.2 for the NASA global precipitation measurement (GPM) integrated multi-satellite retrievals for GPM (I-MERG)* (p. 38). GPM Project.
- Huffman, G. J., Bolvin, D. T., Braithwaite, D., Hsu, K., Joyce, R., Kidd, C., et al. (2020). Integrated multi-satellite retrievals for the global precipitation measurement (GPM) mission (IMERG). In V. Levizzani, C. Kidd, D. Kirschaum, C. Kummerow, K. Nakamura, & F. J. Turk (Eds.), *Chapter 19 in adv. Global change res., Vol. 67, satellite precipitation measurement* (pp. 343–353). Springer Nature. (eBook). https://doi.org/10.1007/978-3-030-24568-9_19
- Hunt, W. H., Winker, D. M., Vaughan, M. A., Powell, K. A., Lucker, P. L., & Weimer, C. (2009). CALIPSO lidar description and performance assessment. *Journal of Atmospheric and Oceanic Technology*, *26*(7), 1214–1228. <https://doi.org/10.1175/2009JTECHA1223.1>
- Jahl, L. G., Brubaker, T. A., Polen, M. J., Jahn, L. G., Cain, K. P., Bowers, B. B., et al. (2008). Atmospheric aging enhances the ice nucleation ability of biomass-burning aerosol. *Science Advances*, *7*(9). <https://doi.org/10.1126/sciadv.abd3440>
- Jiang, H. J., Su, H., Huang, L., Wang, Y., Massie, S., Zhao, B., et al. (2018). Contrasting effects on deep convective clouds by different types of aerosols. *Nature Communications*, *9*(1), 3874. <https://doi.org/10.1038/s41467-018-06280-4>
- Kahn, R. A., Gaitley, B. J., Martonchik, J. V., Diner, D. J., Crean, K. A., & Holben, H. (2005). Multiangle Imaging Spectroradiometer (MISR) global aerosol optical depth validation based on 2 years of coincident Aerosol Robotic Network (AERONET) observations. *Journal of Geophysical Research*, *110*(D10), D10S04. <https://doi.org/10.1029/2004JD004706>
- Khain, A. (2009). Notes on state-of-the-art investigations of aerosol effects on precipitation: A critical review. *Environmental Research Letters*, *4*(1), 015004. <https://doi.org/10.1088/1748-9326/4/1/015004>
- Khain, A., Rosenfeld, D., & Pokrovsky, A. (2005). Aerosol impact on the dynamics and microphysics of deep convective clouds. *Quarterly Journal of the Royal Meteorological Society*, *131*(611), 2639–2663. <https://doi.org/10.1256/qj.04.62>
- Kim, M.-H., Omar, A. H., Tackett, J. L., Vaughan, M. A., Winker, D. M., Trepte, C. R., et al. (2018). The CALIPSO version 4 automated aerosol classification and lidar ratio selection algorithm [Dataset]. *Atmospheric Measurement Techniques*, *11*, 6107–6135. <https://doi.org/10.5194/amt-11-6107-2018>
- Koren, I., Altaratz, O., Feingold, G., Levin, Z., & Reislin, T. (2009). Cloud's center of gravity—A compact approach to analyze convective cloud development. *Atmospheric Chemistry and Physics*, *9*(1), 155–161. <https://doi.org/10.5194/acp-9-155-2009>
- Koren, I., Feingold, G., & Remer, L. A. (2010). The invigoration of deep convective clouds over the Atlantic: Aerosol effect, meteorology or retrieval artifact. *Atmospheric Chemistry and Physics*, *10*(18), 8855–8872. <https://doi.org/10.5194/acp-10-8855-2010>
- Koren, I., Kaufman, Y. J., Rosenfeld, D., Remer, L. A., & Rudich, Y. (2005). Aerosol invigoration and restructuring of Atlantic convective clouds. *Geophysical Research Letters*, *32*(14), L14828. <https://doi.org/10.1029/2005GL023187>
- Koren, I., Martins, J. V., Remer, L. A., & Afargan, H. (2008). Smoke invigoration versus inhibition of clouds over the Amazon. *Science*, *321*(5891), 946–949. <https://doi.org/10.1126/science.1159185>
- Kumar, S., Flores, J. L., Moya-Álvarez, A. S., Martínez-Castro, D., & Silva, Y. (2023). Characteristics of cloud properties over South America and over Andes observed using CloudSat and reanalysis data. *International Journal of Remote Sensing*, *44*(6), 1976–2004. <https://doi.org/10.1080/01431161.2023.2193301>
- Lee, S.-S., Guo, J., & Li, Z. (2016). Delaying precipitation by air pollution over the Pearl River Delta. Part II: Model simulations. *Journal of Geophysical Research Atmospheres*, *121*(19), 11739–11760. <https://doi.org/10.1002/2015JD024362>
- Li, Z., Niu, F., Fan, J., Liu, Y., Rosenfeld, D., & Ding, Y. (2011). Long-term impacts of aerosols on the vertical development of clouds and precipitation. *Nature Geoscience*, *4*(12), 888–894. <https://doi.org/10.1038/NGEO1313>
- Li, Z., Rosenfeld, D., & Fan, J. (2017). Aerosols and their impact on radiation, clouds, precipitation, and severe weather events. *Oxford Research Encyclopedias*. <https://doi.org/10.1093/acrefore/9780199389414.013.126>
- Li, Z., Wang, Y., Guo, J., Zhao, C., Cribb, M. C., Dong, X., et al. (2019). East Asian study of tropospheric aerosols and their impact on regional clouds, precipitation, and climate (EAST-AIRCPC). *Journal of Geophysical Research: Atmospheres*, *124*(23), 13026–13054. <https://doi.org/10.1029/2019JD030758>
- Liu, N., Liu, C., Chen, B., & Zipser, E. (2020). What are the favorable large-scale environments for the highest-flash-rate thunderstorms on Earth. *Journal of the Atmospheric Sciences*, *77*(5), 1583–1612. <https://doi.org/10.1175/JAS-D-19-0235.1>

- Liu, Y., Guha, A., Said, R., Williams, E., Lapierre, J., Stock, M., & Heckman, S. (2020). Aerosol effects on lightning characteristics: A comparison of polluted and clean regimes. *Geophysical Research Letters*, 47(9), e2019GL086825. <https://doi.org/10.1029/2019GL086825>
- Liu, Z., Kar, J., Zeng, S., Tackett, J., Vaughan, M., Avery, M., et al. (2018). Discriminating between clouds and aerosols in the CALIOP version 4.1 data products. *Atmospheric Measurement Techniques*, 12(1), 703–734. <https://doi.org/10.5194/amt-12-03-2019>
- Lohmann, U. (2008). Global anthropogenic aerosol effects on convective clouds in ECHAM5-HAM. *Atmospheric Chemistry and Physics*, 8(7), 2115–2131. <https://doi.org/10.5194/acp-8-2115-2008>
- Mace, G. G., & Zhang, Q. (2014). The CloudSat radar-lidar geometrical profile product (RL-GeoProf); Updates, improvements and selected results. *Journal of Geophysical Research*, 119(15), 9441–9462. <https://doi.org/10.1002/2013JD021374>
- Manoj, M. G., Lee, S.-S., & Li, Z. (2021). Competing aerosol effects in triggering deep convection over the Indian Region. *Climate Dynamics*, 56(5–6), 1815–1835. <https://doi.org/10.1007/s00382-020-05561-3>
- Marchand, R., Mace, G. G., Ackerman, T., & Stephens, G. (2008). Hydrometeor detection using CloudSat-an Earth orbiting 94-GHz cloud radar [Dataset]. *Journal of Atmospheric and Oceanic Technology*, 25(4), 519–533. <https://doi.org/10.1175/2007jtecha1006.1>
- Marengo, J. A., Liebmann, B., Kousky, V. E., Filizola, N. P., & Wainer, I. C. (2001). Onset and end of the rainy season in the Brazilian Amazon Basin. *Journal of Climate*, 14(5), 833–852. [https://doi.org/10.1175/1520-0442\(2001\)014%3C0833:OAEOTR%3E2.0.CO;2](https://doi.org/10.1175/1520-0442(2001)014%3C0833:OAEOTR%3E2.0.CO;2)
- Martin, S. T., Artaxo, P., Machado, L., Manzi, A. O., Souza, R. A. F., Schumacher, C., et al. (2017). The Green Ocean Amazon Experiment (GoAmazon2014/5) observes pollution affecting gases, aerosols, clouds, and rainfall over the rain forest. *Bulletin of the American Meteorological Society*, 98(5), 981–997. <https://doi.org/10.1175/BAMS-D-15-00221.1>
- Mataveli, G. A. V., de Oliveira, G., Seixas, H. T., Pereira, G., Stark, S. C., Gatti, L. V., et al. (2021). Relationship between biomass burning emissions and deforestation in Amazonia over the last two decades. *Forests*, 12(9), 1217. <https://doi.org/10.3390/f12091217>
- McFiggans, G., Artaxo, P., Baltensperger, U., Coe, H., Facchini, C., Feingold, G., et al. (2006). The effect of physical & chemical aerosol properties on warm cloud droplet activation. *Atmospheric Chemistry and Physics*, 6(9), 2593–2649. <https://doi.org/10.5194/acp-6-2593-2006>
- Mielonen, T., Arola, A., Komppula, M., Kukkonen, J., Koskinen, J., De Leeuw, G., & Lehtinen, K. E. J. (2009). Comparison of CALIOP level 2 aerosol subtypes to aerosol types derived from AERONET inversion data. *Geophysical Research Letters*, 36(18). <https://doi.org/10.1029/2009GL039609>
- Morales-Rodríguez, C. A. (2019). Thunderstorm efficiency regimes in South America as observed by STARNET and TRMM. *Journal of Geophysical Research: Atmospheres*, 124(21), 11428–11451. <https://doi.org/10.1029/2019JD030950>
- Morales-Rodríguez, C. A., Neves, J. R., & Anselmo, E. (2011). Sferics timing and ranging network – STARNET: Evaluation over South America. In *Proceedings of the 14th international conference on atmospheric electricity – ICAE*.
- Morales-Rodríguez, C. A., Neves, J. R., Anselmo, E. M., Camara, K. S., Barreto, W., Paiva, V., & Holle, R. L. (2014). 8 years of Sferics timing and ranging NETWORK-STARNET: A lightning climatology over South America. In *23rd international lightning detection conference*. Tucson, Arizona.
- Murray, B. J., O’Sullivan, D., Atkinson, J. D., & Webb, M. E. (2012). Ice nucleation by particles immersed in supercooled water droplets. *Chemical Society Reviews*, 19. <https://doi.org/10.1039/C2CS35200A>
- Niu, F., & Li, Z. (2012). Systematic variations of cloud top temperature and precipitation rate with aerosols over the global tropics. *Atmospheric Chemistry and Physics*, 12(18), 8491–8498. <https://doi.org/10.5194/acp-12-8491-2012>
- Oliveira, R., Maggioni, V., Vila, D., & Morales, C. (2016). Characteristics and diurnal cycle of GPM rainfall estimates over the central Amazon region. *Remote Sensing*, 8(7), 544. <https://doi.org/10.3390/rs8070544>
- Omar, A. H., Winkler, D. A., Vaughan, M. A., Hu, Y., Trepte, C. R., Ferrare, R. A., et al. (2009). The CALIPSO automated aerosol classification and lidar ratio selection algorithm. *Journal of Atmospheric and Oceanic Technology*, 26(10), 1994–2014. <https://doi.org/10.1175/2009JTECHA1231.1>
- Palacios, R. D., Artaxo, P., Cirino, G. G., Nakale, V., Morais, F. G., Rothmund, L. D., et al. (2022). Long-term measurements of aerosol optical properties and radiative forcing (2012–2017) over Central Amazonia. *Atmosfera*, 35(1), 143–163. <https://doi.org/10.20937/ATM.52892>
- Papagiannopoulos, N., Mona, L., Alados-Arboledas, L., Amiridis, V., Baars, H., Biniotoglou, I., et al. (2016). CALIPSO climatological products: Evaluation and suggestions from EARLINET. *Atmospheric Chemistry and Physics*, 16(4), 2341–2357. <https://doi.org/10.5194/acp-16-2341-2016>
- Peng, J., Li, Z., Zhang, H., Liu, J., & Cribb, M. C. (2016). Systematic changes in cloud radiative forcing with aerosol loading for deep clouds from multi-year global a-train satellite datasets. *Journal of the Atmospheric Sciences*, 73(1), 231–249. <https://doi.org/10.1175/JAS-D-15-0080.1>
- Petersen, W. A., & Rutledge, S. A. (2001). Regional variability in tropical convection: Observations from TRMM. *Journal of Climate*, 14(17), 3566–3586. [https://doi.org/10.1175/1520-0442\(2001\)014<3566:rvtico>2.0.co;2](https://doi.org/10.1175/1520-0442(2001)014<3566:rvtico>2.0.co;2)
- Price, C., & Rind, D. (1992). A simple lightning parameterization for calculating global lightning distributions. *Journal of Geophysical Research*, 97(D9), 9919–9933. <https://doi.org/10.1029/92JD00719>
- Protat, A., Bouniol, D., Delanoë, J., O’Connor, E., May, P. T., Plana-Fattori, A., et al. (2009). Assessment of Cloudsat reflectivity measurements and ice cloud properties using ground-based and airborne cloud radar observations. *Journal of Atmospheric and Oceanic Technology*, 26(9), 1717–1741. <https://doi.org/10.1175/2009JTECHA1246.1>
- Randles, C. A., da Silva, A. M., Buchard, V., Colarco, P. R., Darmenov, A., Govindaraju, R., et al. (2017). The MERRA-2 aerosol reanalysis, 1989-onward, Part I: System description and data assimilation evaluation. *Journal of Climate*, 30(17), 6823–6850. <https://doi.org/10.1175/JCLI-D-16-0609.1>
- Remer, L. A., Kleidman, R. G., Levy, R. C., Kaufman, Y. J., Tanre, D., Mattoo, S., et al. (2008). Global aerosol climatology from the MODIS satellite sensors. *Journal of Geophysical Research*, 113(D14), D14S07. <https://doi.org/10.1029/2007JD009661>
- Romps, D. M., Seeley, J. T., Vollaro, D., & Molinari, J. (2014). Projected increase in lightning strikes in the United States due to global warming. *Science*, 346(6211), 851–854. <https://doi.org/10.1126/science.1259100>
- Rosenfeld, D. (1999). TRMM observed first direct evidence of smoke from forest fires inhibiting rainfall. *Geophysical Research Letters*, 26(20), 3105–3108. <https://doi.org/10.1029/1999GL006066>
- Rosenfeld, D., Woodley, W. L., Lerner, A., Kelman, G., & Lindsey, D. T. (2008). Satellite detection of severe convective storms by their retrieved vertical profiles of cloud particle effective radius and thermodynamic phase. *Journal of Geophysical Research*, 113(D4), D04208. <https://doi.org/10.1029/2007JD008600>
- Saad, S. I., da Rocha, H. R., Silva-Dias, M. A. F., & Rosolem, R. (2010). Can the deforestation breeze change the rainfall in Amazonia? A case study for the BR-163 highway region. *Earth Interactions*, 14(18), 1–25. <https://doi.org/10.1175/2010EI351.1>
- Said, R. K., Cohen, M. B., & Inan, U. S. (2013). Highly intense lightning over the oceans: Estimated peak currents from global GLD360 observations. *Journal of Geophysical Research: Atmospheres*, 118(13), 6905–6915. <https://doi.org/10.1002/jgrd.50508>
- Sapucci, C. R., Mayta, V. C., & da Silva-Dias, P. L. (2022). Evaluation of diverse-based precipitation data over the Amazon region. *Theoretical and Applied Climatology*, 149(3–4), 1167–1193. <https://doi.org/10.1007/s00704-022-04087-4>

- Saraiva, I., Dias, M. A. F., Morales, C. A. R., & Saraiva, J. M. B. (2017). Regional variability of rain clouds in the Amazon Basin as seen by a network of weather radars. *Journal of Applied Meteorology and Climatology*, 55(12), 2657–2675. <https://doi.org/10.1175/JAMC-D-15-0183.1>
- Sassen, K., & Wang, Z. (2008). Classifying clouds around the globe with the CloudSat radar: 1-year of results [Dataset]. *Geophysical Research Letters*, 35(4), L04805. <https://doi.org/10.1029/2007GL032591>
- Saunders, C. P. R., Bax-norman, H., Emersic, C., Avila, E. E., & Castellano, N. E. (2006). Laboratory studies of the effect of cloud conditions on graupel/crystal charge transfer in thunderstorm electrification. *Quarterly Journal of the Royal Meteorological Society*, 132(621), 2653–2673. <https://doi.org/10.1256/qj.05.218>
- Schafer, J. S., Eck, T. F., Holben, B. N., Artaxo, P., & Duarte, A. F. (2008). Characterization of the optical properties of aerosols in Amazonia from long-term AERONET monitoring (1993–1995 and 1999–2006). *Journal of Geophysical Research*, 113(D4). <https://doi.org/10.1029/2007JD009319>
- Shan, S., Allen, D. L., Li, Z., Pickering, K., & Lapierre, J. (2023). Machine-learning-based investigation of the variables affecting summertime lightning occurrence over the Southern Great Plains. *Atmospheric Chemistry and Physics*, 23(22), 14547–14560. <https://doi.org/10.5194/acp-23-14547-2023>
- Stephens, G. L., Vane, D. G., Boain, R. J., Mace, G. G., Sassen, K., Wang, Z., et al. (2002). The CloudSat mission and the A-train: A new dimension of space-based observations of clouds and precipitation. *Bulletin of the American Meteorological Society*, 83(12), 1771–1790. <https://doi.org/10.1175/bams-83-12-1771>
- Stolz, D. C., Rutledge, S. A., Piece, J. R., & van den Heever, S. C. (2017). A global lightning parameterization based on statistical relationships among environmental factors, aerosols, and convective clouds in the TRMM climatology. *Journal of Geophysical Research: Atmospheres*, 122(14), 7461–7492. <https://doi.org/10.1002/2016JD026220>
- Stolz, D. C., Rutledge, S. A., & Pierce, J. R. (2015). Simultaneous influences of thermodynamics and aerosols on deep convection and lightning in the tropics. *Journal of Geophysical Research: Atmospheres*, 120(12), 6207–6231. <https://doi.org/10.1002/2014JD023033>
- Storer, R. L., van den Heever, S. C., & L'Ecuyer, T. S. (2014). Observations of aerosol-induced convective invigoration in the tropical east Atlantic. *Journal of Geophysical Research: Atmospheres*, 119(7), 3963–3975. <https://doi.org/10.1002/2013JD020272>
- Sun, M., Li, Z., Wang, T., Liu, D., Qie, X., Mansell, E. R., et al. (2024). Understanding the effects of aerosols on electrification and lightning polarity in an idealized supercell thunderstorm via model emulation. *Journal of Geophysical Research: Atmospheres*, 129(1), e2023JD039251. <https://doi.org/10.1029/2023JD039251>
- Sun, M., Qie, X., Mansell, E. R., Liu, D., Yair, Y., Fierro, A. O., et al. (2023). Aerosol impacts on storm electrification and lightning discharges under different thermodynamic environments. *Journal of Geophysical Research: Atmospheres*, 128(8), e2022JD037450. <https://doi.org/10.1029/2022JD037450>
- Tackett, J. L., Ryan, R., Vaughan, M. A., Garnier, A., Getzewich, B., Winker, D., & Trepte, C. (2022). Mitigation strategy for the impact of low energy laser pulses in CALIOP calibration and level 2 retrievals. In *NTRS-NASA technical report 20220006725, 30th International Laser Radar Conference*. Retrieved from <https://ntrs.nasa.gov/citations/20220006725>
- Tackett, J. L., Winkler, D. M., Getzewich, B. J., Vaughan, M. A., Young, S. A., & Kar, J. (2018). CALIPSO lidar level 3 aerosol profile product: Version 3 algorithm design. *Atmospheric Measurement Techniques*, 11(7), 4129–4152. <https://doi.org/10.5194/amt-11-4129-2018>
- Takahashi, T. (1978). Riming electrification as a charge generation mechanism in thunderstorms. *Journal of the Atmospheric Sciences*, 35(8), 1536–1548. [https://doi.org/10.1175/1520-0469\(1978\)035<1536:reaacg>2.0.co;2](https://doi.org/10.1175/1520-0469(1978)035<1536:reaacg>2.0.co;2)
- Tanelli, S., Durden, S. L., Im, E., Pak, K. S., Reinke, G. D., Partain, P., et al. (2008). CloudSat's cloud profiling radar after two years in orbit: Performance, calibration, and processing. *IEEE Transactions on Geoscience and Remote Sensing*, 46(11), 3560–3573. <https://doi.org/10.1109/tgrs.2008.2002030>
- Tao, W. K., Chen, J. P., Li, Z., Wang, C., & Zhang, C. (2012). Impact of aerosols on convective clouds and precipitation. *Reviews of Geophysics*, 50(2). <https://doi.org/10.1029/2011RG000369>
- Ter Steege, H., Pitman, N. C. A., Sabatier, D., Baralot, C., Salomão, R. P., Guevera, J. E., et al. (2013). Hyperdominance in the Amazonian tree Flora. *Science*, 342(6156). <https://doi.org/10.1126/science.1243092>
- Vaughan, M. A., Powell, K. A., Winkler, D. M., Hostetler, C. A., Kuehn, R. E., Hunt, W. H., et al. (2009). Fully automated detection of cloud and aerosol layers in the CALIPSO lidar measurements. *Journal of Atmospheric and Oceanic Technology*, 26(10), 2034–2050. <https://doi.org/10.1175/2009JTECHA1228.1>
- Veals, P. G., Varble, A. C., Russell, J. O., Hardin, J. C., & Zipser, E. J. (2021). Indications of a decrease in the depth of deep convective cores with increasing aerosol concentration during the CACTI campaign. *Journal of the Atmospheric Sciences*, 79(3), 705–722. <https://doi.org/10.1175/JAS-D-21-0119.1>
- Virts, K. S., Wallace, J. M., Hutchins, M. L., & Holzworth, R. H. (2013). Highlights of a new ground-based, hourly global lightning climatology. *Bulletin of the American Meteorological Society*, 94(9), 1381–1392. <https://doi.org/10.1175/bams-d-12-00082.1>
- Wall, C., Zipser, E., & Lin, C. (2014). An investigation of the aerosol indirect effect on convective intensity using satellite observations. *Journal of the Atmospheric Sciences*, 71(1), 430–447. <https://doi.org/10.1175/JAS-D-13-0158.1>
- Wang, Q., Li, Z., Guo, J., Zhao, C., & Cribb, M. (2018). The climate impact of aerosols on the lightning flash rate: Is it detectable from long-term measurements? *Atmospheric Chemistry and Physics*, 18(17), 12797–12816. <https://doi.org/10.5194/acp-18-12797-2018>
- Wang, Y., Khalizov, A., Levy, M., & Zhang, R. (2013). New directions: Light absorbing aerosols and their atmospheric impacts. *Atmospheric Environment*, 81, 713–715. <https://doi.org/10.1016/j.atmosenv.2013.09.034>
- Williams, E. R., Rosenfeld, D., Madden, N., Gerlach, J., Gears, N., Atkinson, L., et al. (2002). Contrasting convective regimes over the Amazon: Implications for cloud electrification. *Journal of Geophysical Research*, 107(D20), 8082. <https://doi.org/10.1029/2001JD000380>
- Winker, D. M., Pelon, J., Coakley, J. A., Jr., Ackerman, S. A., Charlson, R. J., Colarco, P. R., et al. (2010). The CALIPSO Mission, A global 3-d view of aerosols and clouds. *Bulletin of the American Meteorological Society*, 91(9), 1211–1230. <https://doi.org/10.1175/2010BAMS3009.1>
- Winker, D. M., Vaughan, M. A., Omar, A., Hu, Y., Powell, K. A., Liu, Z., et al. (2009). Overview of the CALIPSO mission and CALIOP data processing algorithms. *Journal of Atmospheric and Oceanic Technology*, 26(11), 2310–2323. <https://doi.org/10.1175/2009jtecha1281.1>
- Wu, M., & Lee, J.-E. (2019). Thresholds for atmospheric convection in Amazonian rainforests. *Geophysical Research Letters*, 46(16), 10024–10033. <https://doi.org/10.1029/2019GL082909>
- Wunderling, N., Staal, A., Sakschewski, B., Winkelmann, R., Tuinenburg, O. A., Donges, J. F., et al. (2022). Recurrent droughts increase risk of cascading tipping events by outpacing adaptive capacities in the Amazon rain forest. *Proceedings of the National Academy of Sciences*, 119(32). <https://doi.org/10.1073/pnas.2120771119>
- Yang, X., & Li, Z. (2014). Increases in thunderstorm activity and relationships with air pollution in southeast China. *Journal of Geophysical Research: Atmospheres*, 119(4), 1835–1844. <https://doi.org/10.1002/2013JD021224>
- Yang, X., Li, Z., Liu, L., Zhou, L., Cribb, M., & Zhang, F. (2016). Distinct weekly cycles of thunderstorms and a potential connection with aerosol type in China. *Geophysical Research Letters*, 43(16), 8760–8768. <https://doi.org/10.1002/2016GL070375>

- Yang, X., Yao, Z., Li, Z., & Fan, T. (2013). Heavy air pollution suppresses summer thunderstorms in central China. *Journal of Atmospheric and Solar-Terrestrial Physics*, 95–96, 28–40. <https://doi.org/10.1016/j.jastp.2012.12.023>
- Yuan, T., Remer, L. A., Pickering, K. E., & Yu, H. (2011). Observational evidence of aerosol enhancement of lightning activity and convective invigoration. *Geophysical Research Letters*, 38(4), L04701. <https://doi.org/10.1029/2010GL046052>
- Zhu, Y., Yu, X., Li, Z., & Rosenfeld, D. (2015). Separating aerosol microphysical effects and satellite measurement artifacts of the relationships between warm rain onset height and aerosol optical depth. *Journal of Geophysical Research: Atmospheres*, 120(15), 7726–7736. <https://doi.org/10.1002/2015JD023547>
- Zipser, E. J., & Lutz, K. R. (1994). The vertical profile of radar reflectivity of convective cells: A strong indicator of storm intensity and lightning probability? *Monthly Weather Review*, 122(8), 1751–1759. [https://doi.org/10.1175/1520-0493\(1994\)122<1751:TVPORR>2.0.CO;2](https://doi.org/10.1175/1520-0493(1994)122<1751:TVPORR>2.0.CO;2)